Eruptive history and magmatic stability of Erebus volcano, Antarctica: Insights from englacial tephra

By

Nels Anton Iverson

Submitted in Partial Fulfillment
Of the Requirements of the
Masters of Science in Geology

New Mexico Institute of Mining and Technology
Department of Earth and Environmental Science

Socorro, New Mexico
November, 2013

Abstract

A tephrostratigraphy of the active Antarctic volcano, Mt. Erebus, was determined from englacial tephra on the ice-covered flanks of Erebus and an adjacent volcano. The tephra are, used to reconstruct the eruptive history and magmatic evolution of Erebus. Scanning electron microscope images and Image Particle Analysis suggest the tephra formed in phreatomagmatic and magmatic eruptions and in some cases both eruptive types are identified in a single mixed tephra. The eruptions forming the mixed tephra likely started as phreatomagmatic eruptions which transitioned into Strombolian eruptions as the non-magmatic water source was exhausted.

We reconstructed the eruptive history of Erebus using the tephra layers stratigraphic position, ^{40}Ar/^{39}Ar ages, shard morphology and grain size. Major and trace element analyses of individual glass shards were measured by electron probe microanalysis and LA-ICP-MS. Trachybasalt, trachyte and phonolite tephra were identified. All phonolitic tephra are Erebus-derived with compositions similar to volcanic bombs erupted from Erebus over the past 40 years. The tephra show that Erebus magma has not significantly changed for 40ka. The uniformity of the glass chemical composition implies that the phonolite magma has evolved by fractionation from a parental basanite and crystallized in the same manner without change throughout the Late Quaternary, suggesting long-term stability of the Erebus magmatic system. Trachyte and trachybasalt tephra were likely erupted from Marie Byrd Land and the McMurdo Sound area, respectively.

Keywords: Erebus volcano, Antarctica, tephrostratigraphy, phonolite, geochemistry, eruptive history, monotonous volcanism

1. Introduction

Ash-sized tephra entrained in glacial ice, either in exposed blue ice fields or in deep ice cores are important repositories for determining an integrated history of Antarctic and global volcanism. Tephra from a single eruptive event can be deposited over wide areas and when correlated can provide excellent time-stratigraphic horizons, especially when the source volcano can be identified (Smellie 1999; Lowe, 2011). Ice is an ideal medium to entrap tephra because even the smallest layers and finest grain sized deposits are easily identified and can be sampled without worries of contamination from the enclosed ice. In Antarctica, tephra found in marine cores (e.g.Hillenbrand et al. 2008; Ross et al., 2012), ice cores (e.g. Gow and Meese, 2005; Dunbar et al., 2011; Narcisi et al., 2012) and blue ice areas around the fringe of the ice sheets (e.g. Keys 1977, Smellie, 1999, Dunbar et al., 2008, Harpel et al., 2008) has been used to determine chronology with which to interpret past climate changes and provide insight into the volcanic history of Antarctica. Acidic volcanic layers in deep ice cores within the Antarctic ice sheets are considered to be responsible for internal reflectors seen by radar and have been used to infer ice sheet stability (e.g. Corr and Vaughan, 2008).

Tephra layers entrained in glaciers on the flanks of Erebus volcano, Antarctica, as well as in blue ice fields found on Ross Island and in the Transantarctic Mountains, provide an excellent record of explosive volcanism from Erebus volcano (Fig. 1). The term tephra loosely defines any ejected material from a volcano (Thorarinsson 1944). Tephra can range in size from extremely fine grained ash of a few microns in diameter to blocks the size of a car (Alloway et al. 2007). Tephra can also be used interchangeably to describe a tephra layer or horizon.

This study examines particle morphology and chemical composition of glass from 35 tephra layers entrained in blue ice areas in order to determine the explosive eruptive history and magma evolution of Erebus volcano. Morphologies of tephra particles were examined to provide insight into past eruptive processes. Image Particle Analysis (IPA) was used to supplement scanning electron microscope (SEM) images to further support eruptive types (e.g. Dellino and La Volpe, 1996; Nemeth et al., 2010; Dürig et al., 2012). The chemical composition of 30 of the 35 tephra layers are similar to present day Erebus anorthoclase-phyric phonolite based on major and trace element glass chemistry. The other 4 tephra layers are not from Erebus and are likely from other volcanoes in Antarctica (LeMasurier and Thomson 1990). Many of the tephra found in blue ice areas occurs in stratigraphic order and a magma evolution was determined for that specific interval of eruptive history. Three tephra layers were dated by the ^{40}Ar/^{39}Ar dating method on anorthoclase separates to provide maximum ages for their deposition.

2. Erebus Volcano

Erebus volcano has grown and evolved over the last 1.3Ma, with eruptive products ranging from basanite to the current anorthoclase-phyric phonolite (Kyle et al., 1992; Esser et al., 2004; Kelly et al., 2008b). Two caldera collapse events, numerous lava flows and an unknown number of explosive eruptions have occurred over the last 100ka. Caldera collapses occurred between 80ka-20ka and between 25ka-11ka (Harpel et al., 2004; Kelly et al., 2008a). Post caldera activity consisted of Strombolian eruptions and lava flows (Panter and Winter, 2008). Strombolian and phreatomagmatic eruptions deposited ash-sized tephra on the flanks of the volcano. Two eruptions were large enough to deposit tephra in the Transantarctic Mountain over 150km from Erebus. One of these ash fall eruption deposits found at Mt. DeWitt has a ^{40}Ar/^{39}Ar age of 39±6ka on anorthoclase feldspar (Harpel et al., 2004). A third distal tephra from Erebus may have been found in the Talos Dome ice core, located ~600km from Erebus (Narcisi et al., 2012). These distal tephra may be associated with the caldera collapses, although evidence is currently lacking to confirm this assertion. During the past 17ka, 13 lava flows have filled the summit caldera forming a broad plateau above 3000m that slopes up to the summit crater (Moore and Kyle, 1987; Harpel et al., 2008).

Erebus has a short and sparse historical record, with detailed observation beginning in 1972. James Ross and members of his expedition described Erebus erupting when they first discovered it in 1841 (Ross, 1847) and infrequent observations were made in the early 1900's by British explorers from their bases on Ross Island (Kyle et al., 1981). Erebus volcano hosts a persistent actively convecting and degassing anorthoclase-phonolite lava lake in its summit crater (Kyle et al., 1992, Oppenheimer and Kyle, 2008). Small infrequent Strombolian eruptions deposit bombs within the 250m deep crater and occasionally outside onto the summit crater rim. In 1984, Erebus underwent a three month period of heightened Strombolian activity, depositing bombs up to 10m in size more than 1 km from the lava lake (Caldwell and Kyle, 1994; Kelly et al., 2008b; Harpel et al., 2008). Another period of elevated Strombolian activity occurred from 2005-2007, with more than 50 Strombolian eruptions per week (Knox, 2012). Visual observations during the Austral summers suggest that ash eruptions are rare; only three have been observed. Two small phreatic eruptions occurred in 1993 and a third ash eruption occurred on December 15, 1997 (Caldwell and Kyle, 1994; Harpel et al., 2008). Although no large ash eruptions have been observed, an excellent ash-sized englacial tephra record is preserved in blue ice areas on the flanks of Erebus volcano.

The chronology of Mt. Erebus's eruptive history is constrained using $^{40}Ar/^{39}Ar$ and ^{36}Cl ages (Kyle, 1992; Esser et al., 2004; Harpel et al., 2004; Kelly et al., 2008a; Simms et al., 2008).

Bombs collected between 1972 and 2007 and samples of lava flows filling the caldera are all phonolite and show that there has been no significant change in composition for the past 17ka (Kyle, 1977; Caldwell and Kyle, 1994; Sumner, 2007; Kelly et al., 2008). Geochemical analyses of glass from englacial tephra on the flanks of Erebus suggest no significant changes in magma composition for the past 36ka, just before which lava chemistry changed from a tephriphonolite to a phonolite (Harpel et al., 2004).

Erebus volcano has an extensive blue ice tephra record. These blue ice areas are small and discontinuous patches whose level of exposure varies from year to year and are often obscured by recent snowfalls. Harpel et al. (2008) conducted geochemical and morphological analysis on 56 tephra layers located on the Barne Glacier, Terra Nova summit and two locations in the Transantarctic Mountains. Two Erebus-derived tephra from the Barne Glacier were dated as 71±5 ka and 15±4 ka (Harpel et al., 2004). Tephra younger than 15ka were not identified in the Barne Glacier section. Harpel et al., (2008) showed from englacial tephra shard morphologies that explosive eruptions at Erebus were typically phreatomagmatic and less commonly from Strombolian eruptions. The distal tephra found over 150km away in the Transantarctic Mountains were thought by Harpel et al. (2008) to be phreato-plinian. There are many other blue ice sections located on the flanks of Erebus with tephra layers that can supplement the early work done by Harpel et al. (2008) and some of these are examined here.

2.1 Field Characteristics

Tephra layers are exposed in almost all blue ice areas around Erebus. Most tephra were collected from blue ice on the flanks of Erebus but some were located on adjacent peaks (e.g.

Mount Terra Nova) and in large blue ice areas in the Transantarctic Mountains (Figs. 1, 2). Blue ice areas represent locations where ablation is occurring. This ablation is cause by wind turbulence on the downwind side of changes in bedrock topography and local ice flow obstructions (Bintanja, 1999; Dunbar et al., 2008) (Fig. 3). These ablated areas may contain tephra layers which define a stratigraphic sequence of volcanic events. Englacial tephra sampled on Erebus appear as thin bands exposed on the surface of glaciers. Surface expressions are usually a thin golden-colored line in the ice and typically have a melt depression down slope of the layer. Some layers show up as depressions in the ice that are formed by melting caused by solar heating of the dark tephra (Fig. 2B). Below the surface, layers are typically 0.5cm to 3 cm in thickness. Very diffuse layers can be much thicker (>1m) but are not easily sampled. They show up as discolored layers in satellite imagery but are difficult to see in the field (Supplemental Data A.2.2). More concentrated ash layers may form small pods (Fig. 2C), which are interpreted to form by surface melting and surface-tension controlled beading of tephra on the depositional snow surface (Fig. 2C). Some layers can be found at the terminus of glaciers and expose a cross-section of the layer (Fig. 2D).

3. Methods

3.1 Samples

Thirty four englacial tephra layers were sampled from the flanks of Erebus, near the summit of Mount Terra Nova and at Allan Hills in the Transantarctic Mountains (Fig. 1) during the 2010-2011 and 2011-2012 Austral summer field seasons. Tephra layers were sampled in stratigraphic order where possible; the lower number is the youngest sample in the unit and the higher number is the oldest sample (Supplemental Data A). Not all tephra are sampled from within a recognizable stratigraphic sequence; these are considered as a single data points. Samples were collected from six main geographic locations which are identified as: TN- Mount Terra Nova summit, DDC-“Dead Dinosaur Cone”, FAP-“False Abbot Peak”, BG- Barne Glacier, MH-Manhaul Bay (Allan Hills) and WE- “West Erebus” (Fig. 1). WE samples were collected from a number of individual locations and are not part of a stratigraphic sequence.

All tephra were sampled from blue or less dense white ice and each layer is assumed to be from a single eruptive event. Reconnaissance samples of tephra-bearing ice were chipped and placed in plastic bags to melt. If the ice contained enough tephra it was re-sampled for geochemical analysis and ^{40}Ar/^{39}Ar dating. Ice containing thicker and more concentrated tephra was sampled by chain sawing out blocks of ice. Ice samples ranging ~25kg to ~360kg were returned to camp, melted, and the tephra were decanted or filtered out and dried.

Seventeen of the tephra layers were mechanically sieved from phi unit 1 to >6 (500 µm to <38 µm) to determine the grain size distribution and the degree of sorting. Samples were weighed for each phi unit and plotted as a weight percent of the total sample volume (Supplemental Data F).

3.2 Image Particle Analysis (IPA)

Image particle analysis was performed using the methods developed by Dellino and La Volpe (1996) and used in many other studies (e.g. Buttner et al., 1999; Zimanowski et al., 2003; Nemeth et al., 2010, Dürig et al., 2012, Lautze et al., 2012). IPA uses different dimensionless particle parameters (Rectangularity, Compactness, Elongation and Circularity) to determine similarities and differences between particles (Durig et al. 2012). Previous studies (Buttner et al., 1999; Nemeth et al., 2010 and Dürig, 2012) have used these parameters to determine the mode of fragmentation and whether or not it is indicative of magmatic or phreatomagmatic fragmentation.

In this study we used Backscatter Electron (BSE) images from a Cameca SX100 electron microprobe for IPA. Images were imported into the imageJ software program and turned into black and white binary images. The binary images made it easier to create a contour (particle outline) of the particles, so measurements could be made (i.e., particle's parameter, area and Feret's diameter). Contours were created using the wand tool to maintain consistent measurements. These parameters allowed for the calculation of rectangularity (defined as the ratio of the particle's perimeter by twice the sum of the particle's breadth and width, where breadth is defined as the distance between the left and right most pixel and width is the distance between the top and bottom most pixel), compactness (the ratio of the particle's area by the breadth and width), elongation (defined as the ratio of Feret's diameter by the mean length within the perimeter perpendicular to the Feret's diameter, Feret's diameter is defined as the longest segment within the particle parallel to the maximum length of the minimum circumscribing rectangle, also called maximum caliper) and circularity (defined as the ratio of the particles parameter by the perimeter of a circle with the same area as the particle) (Fig. 4) (Dellino and La Volpe 1996, Nemeth et al. 2010 and Durig et al. 2012).

Thirty coarse ash layers were chosen for IPA. Ten to twenty particles from each layer were measured and averaged to give a single point for a given sample. Points are plotted on a "Circularity X Elongation" by "Rectangularity X Compactness" graph for IPA determination. IPA graph locations were cross checked with SEM observations and when available, grain size analysis for robustness. Detailed methods and data are given in Supplemental Data C.

3.3 Electron Microprobe Analysis

Volcanic glass from the 35 samples and an internal standard Erebus glass (81003) were measured for major geochemical elements using a Cameca SX-100 Electron Probe Microanalyzer (EMP). Samples were mounted in either a one inch round lucite disk containing 9 holes or a polished 15-sample grain mount thin section. Samples were polished using diamond powder. Because the main target of analysis was Na-rich glass, measurements were made using an electron beam with an acceleration voltage of 15kV and a 10nA beam current. Beam diameter was typically 20µm to minimize the mobilization of Na but in a few samples, where the shards were less than 20 µm, a smaller beam (10µm or 15µm) was required. Ten to 15 pristine glass shards were analyzed in each sample to provide a statistically significant value for each sample. Reference materials VG568 and KN18 were analyzed as part of each microprobe run in order to monitor precision and accuracy of analysis. Individual shard analyses typically totaled between 97 and 102 wt% (Supplemental Data B). These values were normalized to 100% and the mean and RSD are provided for each of the 35 samples (Table 4). Analytical details, as well as analytical precision, are reported in Table 4.

SEM images were collected on the 35 tephra to examine their morphological characteristic to help identify their eruptive mode. Samples were mounted on an aluminum mount adhered with double sided carbon tape and then carbon coated. Samples were imaged with an accelerating potential of 15keV with a beam current of 0.01 nA.

3.4 Laser Ablation-Inductively Coupled Plasma-Mass Spectrometry (LA-ICP-MS)

Trace element analyses were performed by LA-ICP-MS at Aberystwyth University, Wales, UK following the methods of Pearce et al. (2011). Thirty-five samples and Erebus glass standard

81003 were analyzed for 25 trace elements, with ten to fifteen single shards analyzed from each sample. All samples were continuously ablated for ~24s with a 20µm diameter beam from a 193µm Excimer Laser. Calibration was achieved using the NIST612 glass reference material (Pearce et al., 1997) with ^{29}Si used as the internal standard. Full instrument operating conditions are given in Supplemental D.2. Analyses were corrected for gas blanks and instrumental drift. When applicable, LA-ICP-MS analysis was performed on the same glass shard as EMP. The trace element data for each sample were averaged and any analysis outside of two standard deviations of the mean was removed prior to the averages given in Tables 5 and 6. At these conditions typical detection limits for LA-ICP-MS are below 0.1 ppm for most trace elements of interest, except Sr, Ba and Rb which are about 0.5ppm because of instrumental blanks for these elements. Analytical accuracy is typically better than ±5% and precision varies from about ±3% at 100ppm to about ±10% at 10 ppm.

3.5 ^{40}Ar/^{39}Ar Dating Method

Erebus anorthoclase crystals are difficult to date because they are young (<100ka) and contain ~30% melt inclusions, which contain excess ^{40} Ar ($^{40}\mathrm{Ar}_E$). Esser et al. (1997) dated zero age bombs from Erebus that produced ages greater than 200ka. To remedy the effect of $^{40}\mathrm{Ar}_E$, samples must undergo rigorous sample preparation to remove any melt inclusions.

In this study we followed the sample preparation procedures used by Esser et al. (1997) and refined by Kelly et al. (2008a). These samples were magnetically separated using a Franz magnetic separator to remove glass and magnetic minerals. Crystal separates were acid etched in ~15% HF for one hour to remove adhering glass and melt inclusions. Clean crystals were centrifuged in heavy liquid (D=2.65 g/cm^3) to float the anorthoclase crystals. These crystals were crushed to 74-38μm and further acid etched for another 15 minutes. Samples were visually inspected for melt inclusions and were subjected to more acid etching if necessary. Clean samples were placed in copper packets and placed in a 6 hole irradiation tray with Fish Canyon sanidine (FC-2 age =28.02 Renne et al. 1998) monitors interspersed between the samples. Samples were irradiated for one hour at the U.S.G.S Denver TRIGA reactor.

Irradiated samples were dated at the New Mexico Geochronology Research Lab at New Mexico Tech using an Argus VI mass spectrometer in multi-collection mode. Samples were step heated at irregular intervals between 1 W and 10 W by a Photon Machines CO_2 laser with a homogenized beam for 30 seconds (Supplemental Data E has detailed step heating information).

4. Results

4.1 Tephra Characterization

Tephra particle morphologies were characterized for 30 of tephra layers to determine their eruption mechanism (Table 1). Morphologies, vesicularity and grain size vary depending on the nature, size and style of eruption (Heiken and Wohletz, 1985; Sheridan and Marshall, 1983; Harpel et al., 2008; Dellino et al., 2012). Tephra morphologies reported in Table 1 are generally similar to those observed by Harpel et al. (2008). Shards with low to moderate vesicularity have morphologies common to phreatomagmatic eruptions. Shards are typically blocky or platy in appearance with hackly or chipped edges that join together at right angles (Fig. 5A). Mossy particles are common in all of the low to moderate vesicularity deposits. Less common particle morphologies found in these deposits show chemical pitting (Fig. 5B), turbulent shedding (Fig. 5C), hydration rinds (Fig. 5D), quenching cracks (Fig. 5D and 5F), and adhering particles (Fig. 5G). Sublimates and dust aggregates are uncommon (Fig. 5D and 5E, respectively). Accretionary lapilli are rare and were only found in three deposits. Particles that are highly vesiculated are typical of magmatic eruptions. They are dominated by fluidal glassy fragments (Fig. 6F), angular shards (Fig. 6A) and y-shaped bubble walled shards that indicate fragmentation of highly vesiculated glass. Pele's hairs are common (Fig. 6F, 6C, and 6H). Pumice may be present but it is difficult to distinguish pumice from truncated Pele's hair (Fig. 6B). Torn edges (Fig. 6H), fluidal droplets (Fig. 6D and 6E) and budding (Fig. 6D) are less common morphologies that occurred in well vesiculated deposits.

Seventeen tephra were sieved to determine their grain size and sorting statistics were used to infer means of deposition (Supplemental Data F). Thirteen of the 17 tephra have a median grain size >125 μm and 3 are less than 125 μm. One is bimodal (EIT-009). A probability plot of grain size vs. cumulative weight percent (Cas and Wright, 1987) shows that most of the tephra have similar grain size distributions (Fig. 7). Four of the tephra (EIT-009, EIT-010, EIT-012 and EIT-042) are finer grained with median grain size below 3ϕ (125μm). EIT-009 has a bimodal grain size with peaks at 3ϕ and 6ϕ (<63 μm). EIT-020 has a large shoulder in the histogram below 3ϕ and is skewed to the right. The rest of the tephra have similarly shaped Gaussian distributions with small variations in the mean grain size. EIT-013 has a very tight distribution and is the only tephra with a median grain size above 2ϕ (>250 μm).

Inman (1952) sorting parameters ($\sigma_\phi = (\phi_{84} - \phi_{16})/2$) were determined graphically (Fig. 8) from the cumulative weight percent (Table 2). The degree of sorting for Erebus tephra ranges from very well sorted ($\sigma_\phi<1$) to well sorted ($1<\sigma_\phi<2$) (Cas and Wright 1987). Only two samples (EIT-009 and EIT-020) are well sorted. The rest are very well sorted with σ_ϕ between 0.43 (EIT-013, best sorting) and 0.94 (EIT-042). σ_ϕ vs. Md_ϕ is plotted in Fig. 8 to compare Erebus tephra to volcanic deposits previously analyzed by Walker (1971). All of the Erebus tephra plot within the pyroclastic fall field (Fig. 8). Erebus tephra have a smaller Md_ϕ size then most of the particles analyzed by Walker (1971). One sample (EIT-009) lies on the overlapping field of pyroclastic surge deposits. There is no correlation between the degree of sorting and the type of eruption.

4.2 Image Particle Analysis

Image Particle Analysis (IPA) was used to quantitatively analyze tephra shards to accompany the qualitative morphology observations and grain size analysis (Table 3). IPA grain size is based on observations of a small number of individual particles, where the grain size analysis in section 4.2 was based on total weight of the tephra layer. IPA grain size will be an under sampling of the tephra layer. All particles analyzed are ash size (<2mm) tephra, with the largest shard being ~800μm by ~500 μm (EIT-043) and the smallest particle being 12 μm by 10 μm (EIT-042). The median particle size is 145 μm. There is a minor asymmetry in the distribution above ~400 μm. The shoulder is likely from a sampling bias because it is easier to resolve larger particles than smaller ones and no shards were under 10μm were analyzed. More bias is introduced because the ImageJ program is unable to resolve touching particles. Large particles away from other particles are easiest to analyze.

IPA-measured particle distributions and grain shape parameters for all Erebus-derived tephra are shown in Fig. 9. Tephra are broken up into three groups (magmatic, phreatomagmatic and mixed) based on shard morphologies seen in SEM. Compactness values are largest for phreatomagmatic eruptions. Blocky particles, which are a typical phreatomagmatic morphology, will fill their subscribing rectangle more than magmatic and mixed particles. Magmatic and mixed particles are more irregularly shaped and will have smaller compactness values. Magmatic particles have the lowest mean circularity values and phreatomagmatic particles have the highest values. This means magmatic particles are the most irregularly shaped, follow by mixed particles and phreatomagmatic particles. Magmatic particles have the largest peak elongation values with skewing towards larger values. Mixed and phreatomagmatic shards have similar peaks in elongations with skewness toward larger values. All three eruptive types have similar peak values in Rectangularity with skewness toward higher values. Many magmatic particles have higher rectangularity values than the other two eruptive types. This is caused by the irregularly shaped magmatic particles that will have longer parameters than blocky shards of the same size. Magmatic particles have the largest grain size. Mixed and phreatomagmatic particles have similar peaks in grains size with more particles with coarser grain size. Phreatomagmatic particles have a large skewness toward the coarse particles, caused by sampling bias during IPA.

4.3 Tephra Chemical Compositions

The major element compositions of glass shards in 35 tephra are given in Tables 4 and 5. Microprobe analyses were recalculated to 100% and averaged after excluding any outliers outside of two standard deviations of the mean. Although most of the tephra have uniform glass compositions, two tephra from Mount Terra Nova have a bimodal (EIT-001) or mixed (EIT-005) composition (Table 5). EIT-018 from Erebus exhibits a range of phonolite compositions suggestive of a zoned source so no average is provided. The individual analyses are reported in Supplemental Data B.5. For mixed populations, averages are calculated for each distinct composition and are denoted with a letter (e.g. EIT-001b). Averaged trace elements analyses are given in Table 5 and 6. Individual analyses are given in Supplemental Data

4.4.1 Major Element

The glass shards in the tephra show a range of compositions on a total alkali versus silica (TAS) classification diagram. Two are trachybasalts, two trachytes and the majority (30) are phonolitic (Fig. 10). Because the glasses are very similar in 29 of the phonolitic tephra, they are averaged and compared to typical glass in volcanic bombs erupted from Erebus in Table 4. The phonolite glass has an average SiO_2 of 55.60 wt. % and total alkali value of (Na_2O+K_2O) of 14.48 wt. % (Fig. 10). Glasses in the englacial tephra are indistinguishable in composition to the Erebus lava lake, which has an average SiO_2 of 55.74 wt% and total alkali of 14.66 wt.%. Major element variations are typically less than 10% except in MnO, CaO, P_2O_5, SO_2, Cl and F. Most or all of this variation is considered to be analytical (Fig. 11). With the exception of CaO, all of these elements are present at levels of less than 1wt. % so any small variations can appear to be statistically significant. All variations are near to the level of analytical uncertainty.

Small trends can be seen within the stratigraphic sequences at the “False Abbott Peak” area (FAP) and “Dead Dinosaur Cone” (DDC) (Fig. 12). Samples (EIT-020 to EIT-033) from FAP show a subtle decrease (0.05%) in TiO_2 and CaO (<0.1%) as the samples become younger. A small increase in SiO_2 is seen as the layers become younger. DDC tephra (EIT-008 to EIT-015) shows similar trends in TiO_2 and SiO_2 as FAP, but with more scatter in the SiO_2 concentration. Although the chemical variations are very small (barely outside analytical error), the consistence of trends between different analytical elements provides some confidence that the trends are meaningful. This trend has been reported previously and interpreted as due to an increase in clinopyroxene fractionation (Kyle et al., 1992).

4.4.2 Trace Elements

Thirty-two tephra layers were analyzed for 25 select trace elements. Glass in 30 of the phonolitic tephra are chemically uniform in terms of trace elements. One phonolitic tephra has variable trace elements (EIT-018) and one layer is a trachybasalt (EIT-003) (Table 5 and Table 6). Trace elements in the 30 phonolitic tephra vary by less than 20% (2σ) from the mean on all trace elements, except for Pb which has 21.4% (2σ) variation from the mean. The light rare earth elements (LREE) have less scatter (8%-13% at 1σ). Heavy rare earth elements (HREE) have more scatter (8%-20% at 1σ), which is the analytical precision for concentrations of ~1ppm. The LREE are more incompatible compared to the HREE (La_n/Yb_n=18.1-21.4). The greatest concentration variations are seen in trace elements that are highly incompatible with feldspar (e.g. Zr (1394-1710ppm) or compatible Sr (201-326ppm)). Incompatible element ratios (Nb/Ti, Nb/U, Zr/Rb and Lu/Hf) of the glass shards are consistent with the values seen in Erebus bombs and lava flows (Kelly et al. 2008b).

When normalized to a parental-like trachybasalt (EIT-003), depletion is seen in Sr, Ba, Eu, and Pb, while the rest of the REE are enriched in comparison (Fig. 13). EIT-003 is not considered the parental melt for which Erebus phonolites are derived, but is merely used due to similar composition and analytical conditions. Basanites and trachybasalts are common in Erebus volcanic province and EIT-003 is used as a proxy for regional mantle composition (Keys, 1977). The depletion of Sr and Ba is caused by removal of feldspar during fractional crystallization (Kyle et al., 1992).

4.2.3 Mount Terra Nova

The blue ice area at the summit of Mt. Terra Nova contains the most diverse range of tephra found in this study. Of the seven layers sampled from the summit blue ice area, two are phonolitic (EIT-004 and EIT-006), one is trachybasaltic (EIT-003), one is trachytic (EIT-007) and two contain a mixture of basanite, trachybasalt, phonolite and trachyte glass shards (EIT-001 and EIT-005). The mixed deposits are grouped by composition, averaged and denoted by a letter (Table 6). The two mafic tephra differ in composition. EIT-001a (SiO_2 44.01 wt. % total alkali 6.60 wt. %) has a lower abundance of SiO_2, MgO and CaO than EIT-003 (SiO_2 45.54 w. % and total alkali 5.52 wt. %). EIT-001a has higher concentrations in all other major elements (TiO_2, Al_2O_3, FeO, MnO, Na_2O, K_2O, P_2O_5, F, and Cl) with the greatest difference in TiO_2, FeO and K_2O. The phonolites (EIT-001b, EIT-004, EIT-005a and EIT-006) have very similar compositions to the phonolites from the flanks of Erebus. The trachytic tephra EIT-007 has a SiO_2 content of 63.12 wt. % and total alkali of 11.58 wt %. Other trachytic glass found in mixed tephra (EIT-005b and c) differ most in SiO_2, TiO_2, FeO, CaO and Na_2O and have near identical MnO and K_2O. All of the trachytes are very low in MgO and P_2O_5.

4.4 ^{40}Ar/^{39}Ar Dating

Maximum eruptions ages were determined for two of the three tephra layers dated (Fig. 14). Two samples (EIT-015 and EIT-008) were from “Dead Dinosaur Cone” (DDC) and one sample (EIT-034) was from “West Erebus” (Analytical data in Supplemental Data E). EIT-008 and EIT-015 are from the top and bottom of the stratigraphic sequence, respectively, and were dated to bracket the age of the 8 tephra exposed at DDC. A 1.3mg aliquot of anorthoclase feldspar from EIT-008 produced a preferred plateau age of 40±20ka (Fig. 14A). The spectrum started young (Step B) and became progressively older with each step (B-E). The last steps (F-N) have large errors and an irregular shape caused by low gas yield (last 20% of gas released). Radiogenic yields for the gas fractions making up the plateau were between 13 and 36%. Most age spectra showed an increase in age, radiogenic yield and uncertainty after ~70% of gas was released. EIT-015 produced a plateau age near 1Ma, too old for Erebus phonolites. Two aliquots of the four laser heated aliquots from EIT-034 produce statistically similar ages. EIT-034-03 maintained a semi-flat spectrum throughout the heating schedule and produced an age of 36±10ka, with radiogenic yields less than 7% (Fig. 14C and 14D). EIT-034-04 was analyzed by the multi-hole aliquot method and produced the youngest plateau observed at 31±7ka. This plateau encompasses ~50% of the gas released and has a low but steady ^{40}Ar* yields between 8% and 17%. The last 50% of the spectra is very disturbed and have varying Cl/K concentrations and ^{40}Ar* yield. This occurs at higher temperature and is most likely from degassing of melt inclusions that contain Cl and $^{40}Ar_E$ (Esser et al., 1997).

Isochron ages were used to check for age consistency with ages produced by age spectra. EIT-008, with a preferred plateau age of 40±20ka, had an inverse isochron age of 50±10ka, which is indistinguishable at 2σ (Fig. 14B). The inverse isochron has large error ellipses due to the large error associated with the ^{36}Ar measurement. These error ellipses help reduce the MSWD to 4 and have a $^{40}Ar/^{36}Ar$ intercept of 297±9, showing no trapped atmospheric component. EIT-034-03 gave inverse isochron ages of 34±11ka and had an MSWD of 1.9 with a$^{40}Ar/^{36}Ar$ ratio of 300±40 (Fig.14E). EIT-015-05 had too much scatter in apparent age due to excess ^{40}Ar, so an inverse isochron was not produced.

5. Discussion

5.1 Eruptive Mechanism

Particle morphologies from Erebus phonolites have been categorized into three different groups: phreatomagmatic, magmatic and mixed eruptions, similar to interpretations of Harpel et al. (2008) (Table 1). Five of the tephra analyzed exhibit morphologies suggesting they formed in purely phreatomagmatic eruptions. They are dominated by brittle fragmentation and form distinctive morphologies dominated by blocky or platy particles that are poorly vesiculated (Sheridan and Woheltz 1987; Büttner et al., 2002; Zimanowski et al., 2003). Mossy and hackly particles are common morphologies for phreatomagmatic tephra. Büttner et al. (2002) have seen these textures in natural and experimental particles and attribute annealing of the particle after brittle fragmentation to the irregular shape of the mossy particles. Hydration rinds, chemical pitting and quenching cracks are caused by chemical and mechanical processes that affect the surface of the glass (Heiken and Wohletz 1985; Büttner et al., 2002). Fine grained adhering particles are common and are indicative of phreatomagmatic eruptions (Heiken and Wohletz 1985). Many shards have chipped edges that may have been caused during fragmentation of the melt (Büttner et al., 2002; Dellino et al., 2012) or by eolian processes during deposition.

Fifteen of the tephra layers have shard morphologies typical of magmatic eruptions. These shards are dominated by fluidal glass, Pele's hair and Y-shaped septa. These morphologies are formed by ductile fragmentation during the eruption (Büttner et al., 2002). Pele's hairs can be >500 μm in length and may be a single elongated vesicle or multiple elongated vesicles that would resemble a pumice clast if truncated. Many shards have torn edges and blown out vesicles likely caused by gas expansion after the glass particle cooled and became more viscous. Spherical to sub-rounded melt droplets are rare but do occur in several tephra. Some melt droplets may have several smaller droplets adhering to the main droplet. This is known as ash budding and occurs during coalescence of small pyroclasts or disaggregation of a larger melt globule (Harpel et al., 2008).

Thirteen of the tephra contain both magmatic and phreatomagmatic morphologies. These tephra are considered a mixture of the two eruptive types. A mixed deposit would likely occur during a transformation from phreatomagmatic to magmatic eruption as the external water source during the phreatomagmatic activity was exhausted. Typically this evolution is seen at volcanoes where water is readily available as ground water or sea water (e.g. Surtsey (Thorarinsson, 1966), Tolbachik (Doubik and Hill, 1991), Tenerife, Canary Islands (Clarke et al., 2009) and Okmok (Wong and Larsen, 2010)). Magmatic particles may also be present in deposits thought to be purely phreatomagmatic. La Fossa on Vulcano, Italy, has been known to deposit phreatomagmatic particles and Pele's hair and Pele's tears during the same eruption (Büttner et al. 2002). This transition has been seen recently in glacier covered volcanoes like the 2010 Eyjafjllajökull eruption where the eruption was initially dominated by water-magma interaction from the melting glacier and then moved toward a dry magmatic eruption once the glacial water no longer came in contact with the melt (Dellino et al. 2012). Currently, the Erebus summit crater is not covered by ice and snow, so it is difficult to understand a phreatomagmatic eruption occurring, but it is likely that periods of quiescence have occurred in the past, allowing the summit crater to fill with ice and snow and then during the next eruption there would be enough water to cause phreatomagmatism. Another possibility for phreatomagmatism at Erebus would be an avalanche of snow and ice into the active lava lake, like one reported in 1997 by Rowe et al. (2000). This event did not trigger one large eruption but several hundred very small bubble bursts caused by vaporizing snow and ice. This event produced very little tephra (Harpel et. al 2008) and a much larger block of ice and snow would be required to produce a large phreatomagmatic eruption. Mixture of tephra from multiple eruptions within a single tephra layer, due to eolian reworking must also be considered as some of the tephra exhibit multiple geochemical signatures (e.g. EIT-001a and EIT-001b in Table 6).

Phreatomagmatic eruptions tend to form a greater proportion of fine grained ash than magmatic eruptions (Walker and Crosdale, 1971; Heiken and Wohletz, 1985). All of the tephra layers, except EIT-042, are found within 15km of the summit. At this distance all phreatomagmatic tephra have a mean grain size distribution <125 µm, whereas magmatic tephra have a mean grain size distribution >125 µm (Fig. 7). Volcanic ash with most of their grain size below 100-200 µm is typically considered to be phreatomagmatic in proximal deposits (Zimanowski et al., 2003). Mixed Erebus tephra layers either have a bimodal grain size distribution or they have ~50% of the particle distribution above 125 µm and ~30-40% of the particle distribution between 125 µm and 63 µm. EIT-042 is the only distal tephra sampled and it does not have any glassy particles >110 µm and has a very asymmetrical grain size distribution. The few particles that are >110 µm are windblown lithics from the surrounding outcropping rocks.

Particles found in EIT-003 are typically platy and sometimes blocky, but do not exhibit any other particle morphologies that are considered phreatomagmatic (e.g. mossy or quenching cracks). There are particles indicative of ductile fragmentation which are stretched and elongated. While most of the shard morphologies are consistent with Strombolian morphologies, it is possible that this eruption could have a different eruption type because EIT-003 is trachybasaltic and would be derived from much less viscous melt. EIT-007 is very fine grained and consists of platy and elongated shards. EIT-007 is also given the magmatic eruptive style because it is a trachyte and would likely have a more explosive eruptive type. It is not given a Plinian or Vulcanian eruption type due to the lack of pumice (Heiken and Wohletz, 1985).

5.2 Quantifying Eruption Mechanism

Magmatic and phreatomagmatic fragmentation regions are graphically determined based on SEM imagery for all tephra analyzed by IPA. Higher Circularity and Elongation better suggest ductile (magmatic) fragmentation whereas higher Rectangularity and Compactness suggest brittle fragmentation (water-magma interaction). Fragmentation regions (Fig. 15) for magmatic and phreatomagmatic eruptions are in good agreement with eruptive mechanisms inferred from morphological characteristics seen in SEM images. Derived particle parameters (Rect*Comp and Circ*Elong) on individual particles were averaged together to determine mean values for each tephra layer (Fig. 15).

Tephra layers from phreatomagmatic eruptions, based on SEM images, tend to plot in the lower right hand quadrant of Fig. 15. Phreatomagmatic fragmentation occurs within the brittle regime of the melt and does not require vesicles to be present in order to fragment the melt (Büttner et al, 2002). These particles will be more equant and blocky in shape with irregular edges resulting from direct contact with water (Büttner et al., 1999; Dellino et al., 2012). Phreatomagmatic tephra have much higher mean distribution for Compactness (0.56) and a multi-modal distribution for Rectangularity (Fig. 9). Circularity and Elongation have lower values for magmatic tephra (2.5 and 3.1, respectively) (Fig. 9). Magmatic tephra have the smallest Circ*Elong values and the largest Rect*Comp values, with the exception of EIT-010. EIT-010 is considered to be the phreatomagmatic based on particle morphologies, yet it has high

Circ*Elong values and low Rect*Comp values. This is likely caused by a sampling bias during IPA. Particles that look magmatic were chosen over blocky particles to reduce the chance of performing IPA on feldspars. The ImageJ program cannot resolve touching particles and therefore spatially isolated particles were used. These individual particles may not be indicative of the whole layer and thus a bias is created. Erebus tephra have a lower Rect*Comp value (average=0.44) compared to other published values (Buttner et al. 2002). This puts all Erebus tephra layers within the ductile zone where Rect*Comp values <~0.85 (Fig. 6 from Büttner et al. (2002)). In fact Erebus has very few particles (25 of 504 particles analyzed) that have a Rect*Comp above 0.80 (Supplemental Data C), suggesting that Erebus does not undergo pure magma-water fragmentation during a given eruption and that ductile fragmentation is still an important component of the fragmentation process. Particles that have quenching cracks or mossy textures would have formed under conditions where fragmentation had both brittle and ductile components (Büttner et al. 2002).

Magmatic tephra are in the upper left quadrant of the Rect*Comp by Circ*Elong plot (Fig. 15). Circularity and Elongation have higher mean values, 3.08 and 4.23 respectively, than phreatomagmatic and mixed tephra, with some asymmetry toward higher values (Fig. 15). Rectangularity values are similar (~1) for all eruptive types. On the other hand, magmatic tephra layers have much lower Compactness values (average 0.44) than mixed and phreatomagmatic layers. This lower value reduces the significance of Rectangularity and cause all of the Rect*Comp values to be <0.45.

Mixed eruptions typically have values between the two end member eruptions types creating a spectrum between the most magmatic tephra layer (EIT-036) and the most phreatomagmatic layer (EIT-018) (Fig. 15). Mixed eruptions that overlap with phreatomagmatic and magmatic tephra layers are caused by the sampling bias discussed above. Mixed eruptions typically fall near the intersection of the two perpendicular lines on the plot.

5.3 Erebus Matrix Glass Evolution

A comparison of Erebus phonolitic glass from englacial tephra to matrix glass from lava bombs collected between 1972-2005 shows very little chemical variation (Table 4 and Table 5). Kelly et al. (2008b) compared the lava bomb data to intra-caldera lava flow glass chemistry (Caldwell and Kyle 1994) and saw the same chemical consistency over the past ~17ka. These data are also consistent with glass chemistry from different englacial tephra sites studied by Harpel et al. (2008). In all, over 100 different tephra (bombs and ash) from Erebus have been analyzed (56 from Harpel et al. (2008), 30 from Kelly et al. (2008b) and 34 from this study) and all of the chemical compositions agree within the total variation of the data (Fig. 16). The trace elements were analyzed by two different ICP-MS methods. Kelly et al., (2008b) used solution ICP-MS and in this study we used in situ laser ablation ICP-MS. Even with two different methods of trace element analysis, Erebus glass composition has remained stable over an extended time period regardless of eruptive product (i.e. lava flow matrix glass, bombs, ash). The largest variations in major and trace elements are observed for K_2O, Na_2O, CaO, Rb, Sr, Ba (Fig.16), suggests that the level of crystal fractionation (anorthoclase feldspar, pyroxene, and apatite) may vary over time. Anorthoclase feldspar represents on average ~30% of the bulk magma (Kyle et al, 1977; Kelly et al. 2008b), and pyroxene and apatite are present at lower abundances. The bulk CaO content of glass shows the most variability with ~10% variation among samples analyzed in the study, which could be related variation in the amount of anorthoclase, pyroxene and apatite in the magma. CaO may be particularly strongly affected by the melt-crystal balance because it is strongly compatible in pyroxene and apatite. Sr has similar variability (~9%) as CaO, which it readily substitutes into the Ca site. K_2O and Na_2O, which will be largely controlled by anorthoclase, and for which the melt to crystal concentrations are fairly close, have <2% variation. Ba and Rb have less variability (~4%), similar to K_2O. The rest of the trace elements show less than 10% variation. Elements that are affected by crystal fractionation may either be replenished by a new influx of melt or episodes of phenocryst resorption may allow the melt to return to its original composition. The former seems a simpler mechanism for maintaining the monotonous phonolite composition found at Erebus, even though recurrent resorption episodes are observed in many anorthoclase (Dunbar et al., 1994; Sumner, 2007). The influx of new magma is further supported by the need for a parental basanite to be emplaced at depth to account for the constant high levels of CO_2 and magmatic water being degassed from the lava lake (Oppenheimer et al., 2009).

The lack of microlite crystals in glass shards found in englacial tephra further supports a long lived open system. Microlites tend to occur during shallow crystallization and may form minerals much different than the minerals that crystallize deeper within the magma chamber, thus making residual melt more evolved (Cashman, 1992; Streck et al., 2005). Microlitic textures can be attributed to vent clogging during an eruption (Streck et al., 2005). If vent clogging occurred during an eruption at Erebus, microlites may have enough time to form and modify the surrounding glass chemistry. At Erebus volcano, even across products from several types of eruptive mechanisms, microlites were rarely seen. This observation supports the presence of a long-lived open conduit system where material can freely exchange from the near surface back into the magma chamber (Calkins et al., 2008) without microlitic growth. Dunbar et al. (1994), suggests that a lack of nucleation sites may also play a role in controlling the lack of microlites and the normal distribution of large anorthoclase phenocrysts. It is easy to speculate that, with

~30% anorthoclase in the melt and a lack of nucleation sites, new growth would occur at the boundary layer surrounding anorthoclase crystals, but this phenomena has not been seen (Kelly, et al. 2008b). The lack of a boundary layer is further supported by the similarity of melt inclusion data to that of matrix glass (Kyle et al. 1977; Dunbar et al., 1994). No boundary layers would suggest a well mixed magma chamber that homogenizes quickly or that crystal growth is slow to allow homogenization. Figure 17 shows the evolution of the melt over time, based on stratigraphic relations from two different parts of the volcano. The chemical variations of Na-K do not show any trend with time, instead the values change somewhat cyclically around the Erebus mean concentration (Fig. 17). Note that an increase in K_2O does not mean a decrease in Na_2O or vice versa. The same phenomena can be seen in the trace elements with Rb and Sr, which readily substitute into anorthoclase. The random decrease and increase in major and trace elements concentrations about the mean Erebus composition means that the magma chamber is extremely stable and minor changes in concentration can be accounted for by minor feldspar fractionation or accumulation. Anorthoclase from Erebus phonolites have compositional zonations at a similar magnitude as glass compositions. K_2O in anorthoclase vary by ~0.2 wt. % and Na_2O varies by ~0.6 wt. % (Sumner, et al., 2007), which approximately twice the variation seen in phonolite glass.

5.4 Distal Erebus Tephra

Three distal tephra found entrained in blue ice in the Transantarctic Mountains are geochemically similar to present day Erebus phonolites (Harpel et al., 2008) (Figure 1). Two of these tephra (BIT-272 and BIT-288) are from Mt. DeWitt (MD) and another tephra (BIT-42 and re-sampled in this study, EIT-042) from Manhaul Bay in the Allan Hills (Table 8). EIT-042 from

Allan Hills is the finest grained sample (Md_ϕ ~ 4) in this study, where all particles are less than 110μm. The fine grain size and Erebus phonolite chemical composition for EIT-042 are consistent with observation made by Harpel et al. (2008). This tephra is very blocky. The fine grained and blocky nature of the deposit is typical of phreatomagmatic eruptions. Harpel et al. (2008) speculated that this eruption was perhaps phreato-plinian because of its widespread dispersion. There is no new evidence to dispute this and therefore it is likely that EIT-042 was from a large phreato-plinian eruption. Narcisi et al., (2012) suggested a tephra in the Talos Dome ice core was from Erebus. Most oxides compositions of the Talos Dome tephra are outside of the mean Erebus composition (SiO_2 is ~3 wt. % larger, Na_2O is ~1 wt. % higher and FeO, Al_2O_3 and K_2O are ~1wt. % lower). Because of its very small grain size the Talos Dome tephra was analyzed by energy dispersive X-ray spectrometry (EDS) and all analyses have large errors (>1wt. %) (Narcisi et al., 2012). Taking into account the large analytical errors we cannot completely rule out Erebus as a possible source of the tephra but higher precision analyses are needed to allow a strong correlation.

5.5 Eruptive history

The eruptive history of Erebus is dominated by Strombolian and phreatomagmatic eruptions with less frequent lava flows. The two new $^{40}Ar/^{39}Ar$ ages of englacial tephra layers fall within the previously determined phonolite phase of Erebus, lasting the past ~36ka (Harpel et al. 2008). EIT-008 is at the top of "Dead Dinosaur Cone" and represents the youngest tephra found in blue ice on the Terra Nova Glacier at 40 ±20 ka. This is considered to be a maximum age for the top of the DDC blue ice area. Erebus anorthoclase contain ~30% melt inclusions, which are riddled with excess argon ($^{40}Ar_E$) (Esser et al., 1997; Esser et al. 2004; Harpel et al., 2008; Kelly et al., 2008a). This $^{40}Ar_E$ can cause the sample to have a much older apparent age, even when the percent of melt inclusions is ~1%. The youngest plateau age for EIT-034 is 31±7 ka and is also considered a maximum age. EIT-034's elevation is approximately half way between the two Harpel et al. (2008) samples dated at 15ka and 71ka. The 71ka age is considered to be contaminated by xenocrysts (Harpel et al, 2008). The tephriphonolite lava flows on the north side of the Barne glacier are dated at less 40±6ka (Esser et al., 2004). This means the age of the tephra from the terminus of the Barne Glacier is more likely to be less than 40ka, which would be consistent with the tephriphonolite-phonolite transitions that Erebus underwent ~36ka (Esser et al., 2004; Harpel et al., 2008).

Harpel et al. (2008) dated one distal tephra from Mt. DeWitt in the Transantarctic Mountains at 39±6ka. Based on glass chemistry, the Mt. DeWitt tephra has a glass composition that is the same as the present day Erebus anorthoclase phonolite (Harpel et al. 2008). It is highly likely that Erebus has been geochemically stable for the past ~40ka when it evolved from a tephriphonolite to a phonolite. The new tephriphonolite-phonolite transition age still conforms to the youngest tephriphonolite date of 37±14 for the Cape Evans lava flow (Esser et al. 2004). Further dating of englacial tephra and summit lava flows would be useful in confirming the age of the transition between tephriphonolite and phonolite.

5.5 Monotonic Volcanism

Most volcanic systems have a diverse chemical history explained by discreet pulses of magma that geochemically evolve over time. Erebus is no exception; it evolved from a parental basanite to the current phonolite (Kyle et al., 1981, Harpel et al,. 2008). However, over the past

<40ka Erebus has remained chemically uniform. Other examples of chemically monotonic volcanism have been seen in different volcanic terrenes (e.g. Kilauea (Marske et al., 2008); Arenal, Costa Rica (Streck et al., 2005); Damavand, Iran (Davidson et al., 2004); Mt. Erciyes, Turkey (Dogan et al., 2011)), but reasons for the homogeneities are not well understood.

Major element chemistry from Kilauea is fairly stable with the exception of MgO which can vary from ~6.7 to ~10%, as a result of olivine fractionation (Marske et al., 2008). Erebus undergoes a similar variation caused by anorthoclase crystallization but does not vary as much from the mean composition. Mantle heterogeneities have been recognized through study of trace elements at Kilauea, where different stages of an eruption (e.g. the current Pu'u O'o eruption) tap discrete portions of a heterogeneous Hawaiian plume (Marske et al, 2008). These heterogeneities at Kilauea occur over short time scales (months to years) where Erebus trace elements have been chemically monotonous for 1000's to 10,000's of years. Damavand volcano in Iran has been chemically homogenous (59-62wt. % SiO_2 and 8.0-10 wt. % total alkalis) during its entire history (~1.8Ma) with no compositional trends over time (Davidson et al. 2004). Damavand is a composite volcano not associated with a hot spot like Erebus or Kilauea but does provide some insight into long lived monotonous volcanism. Mt. Erciyes is a stratovolcano, whose summit is comprised of several compositionally homogenous dacite lava flows that rival the chemical homogeneity found on Erebus. The whole rock chemistry of these dacite lava flows varies <10% in regards to both major and trace elements (Dogan et al., 2011). These dacites have not been directly dated and are poorly constrained by K-Ar, ^{14}C and exposures ages to have been erupted during the past 0.9 Ma, but are more likely to have been erupted between 140ka and 10ka (Dogan et al., 2011). Arenal has been chemically stable for the past 30 years but it does have a more complex mineralogy that causes slight variations over longer time periods (Streck et al.

2005). The complex mineralogy is attributed to tapping slightly different melts at depth. Erebus phonolite is thought to undergo less complex crystallization, dominated by anorthoclase, with lesser contributions by pyroxene, apatite, magnetite and olivine (Kyle, 1977).

5.7 Mt. Terra Nova and Non-Erebus Derived Tephra

Six of the tephra layers from the summit of Mount Terra Nova were analyzed and include compositions unlike any observed in other tephra from blue ice areas on Ross Island. Three of the tephra have phonolitic glass compositions similar to current Erebus phonolite (Table 6). Glass from EIT-001b is similar to typical Erebus glass, but some glass shards are basanitic and heterogeneous (Supplemental Data B 5.1). Three tephra layers have trachybasalt and trachyte glass compositions (Fig. 10) unlike any recent eruptive products from Erebus and must have been erupted from other volcanic sources. Glass found in EIT-005 has three distinct populations. One is phonolitic, similar to Erebus and two are trachytic (Fig. 10; Table 6). EIT-007 is a uniform trachyte tephra. Trachytes are un-common volcanic products at Erebus and the only known occurrences were erupted between 157ka and 166ka (Esser et al., 2004; Kelly et al., 2008). There are no known young trachytic eruptions in the McMurdo Sound area (Kyle, 1990c). Trachytic eruptions are common in Victoria Land at Mt. Melbourne and The Pleiades (Kyle, 1990b; Esser and Kyle, 2002; Narcisi et al., 2012) and in West Antarctica (Mt. Berlin and Mt Takahe) (Palais et al., 1988; Dunbar et al, 2008, 2011). Based on major element chemistry Mt. Melbourne and The Pleiades are likely not the source for these trachytic tephra (Table 7). The Pleiades and Mt. Melbourne have lower FeO and higher MgO than the Mt. Terra Nova trachytes (Kyle, 1982; Worner et al., 1989; Esser and Kyle 2002). Mt. Takahe is another possible source volcano but it has had fewer eruptions during the past 40ka than Mt. Berlin (Palais et al., 1988; Dunbar et al. 2008). The homogenous trachytic tephra (EIT-007) at Mt. Terra Nova is distal (particles <10μm) and based on the glass composition the most likely source is Mt. Berlin. EIT-007 is geochemically similar to Mt. Berlin's BIT-152 found at Mt. Moulton (Dunbar et al., 2008). All major elements, with the exception of Na_2O, are statistically the same as BIT-152. The Na_2O is low because shards in EIT-007 were analyzed with 10μm beam which can cause Na loss. An identical trachytic tephra is also found in the Siple Dome core (SDMA-5683) and the new West Antarctica Ice Sheet divide core (WDC06A) (Dunbar, unpublished data). In the Siple Dome core this trachyte tephra is dated at 28.5ka by counting snow accumulation layers (Taylor et al., 2004). Based on the glass compositions we therefore believe that EIT-007 is 28.5ka and provides the first age for the ice at Mt. Terra Nova summit. The fact that trachytic tephra EIT-007 is found at several locations in West Antarctica and now on Ross Island means that it may be an important marker and is a potential link between West Antarctic and East Antarctic ice cores. EIT-007 is located at the bottom of the section found at Mt. Terra Nova, making all of the tephra found at Terra Nova Summit less than 28.5ka, suggesting that the Terra Nova summit blue ice site could potentially provide a climate record across the last glacial maximum . EIT-006 is an Erebus phonolite located ~40m above EIT-007, providing another maximum age constraint on the current eruptive phase at Erebus. The correlation age of EIT-007 is consistent with the age of known activity on Mt. Erebus outlined earlier.

The trachybasaltic glass (EIT-003) and the few basanitic shards in EIT-001 are likely to be from a local source because they are coarser than the trachytes but finer grained than the Erebus phonolites found at Mt. Terra Nova. Mafic eruptive products in the Erebus volcanic province are typically alkali basalts, basanites and less common trachybasalts. These mafic eruptions typically form scoria cones and have Hawaiian to Strombolian eruptive styles, which do not disperse tephra far from the vent (Keys et al., 1977). Basanites found on Ross Island are much older (>400ka) than the current phonolitic phase on Erebus (Kyle, 1990b). The trachybasalt and basanite tephra are found towards the top of the Terra Nova Summit section and are therefore younger than the correlated trachyte tephra (<28.5ka). Young mafic volcanic are found on the eastern front of the Royal Society Range <150km from Terra Nova (Wright and Kyle, 1990). Other basanitic tephra in ice in Southern Victoria land are estimated to be <20ka (Keys et al., 1977). A few basaltic cones at Mount Morning are also <20ka (Paulsen and Wilson, 2009; Martin et al., 2010). As the prevailing wind is from the south it is reasonable to assume that the trachybasalt and basanite tephra had a source in southern McMurdo Sound.

6. Conclusions

1) The vast majority of englacial tephra layers exposed on the flanks of Mt. Erebus and in the summit area of nearby Mt. Terra Nova, as well as some englacial tephra layers at Mt. DeWitt and the Allan Hills, have phonolitic compositions that indicate they were erupted from Mt. Erebus. Also present at Mt. Terra Nova are basanitic and trachybasaltic tephra probably erupted from southern Victoria Land and trachytic tephra from Mt. Berlin in West Antarctica.

2) Glass from 29 englacial phonolitic tephra layers on the flank of Erebus volcano some dated to approximately 40ka, have compositions similar to the matrix glass of bombs erupted from the persistent lava lake at Erebus. The major and trace element composition of the magmatic system has remained unchanged for the past ~40ka.

3) SEM images on phonolitic glass shards show Erebus has produced a wide variety of particle morphologies. The different types of particles are typical of magmatic and phreatomagmatic eruptions. Some of the tephra layers exhibit both magmatic and phreatomagmatic shard morphologies and are interoperated to be produced by mixed eruptions. These eruptions likely occurred after a period of quiescence where a summit crater would fill with ice and snow. Once the volcano began to become more active, it would melt the ice and snow and this would create phreatic eruptions and then eventually phreatomagmatic eruptions. Once the water was exhausted, the eruption would become more magmatic and the mixing of different fragmentation modes occurred.

4) Quantitative particle analysis of phonolitic glass shards has helped identify both magmatic and phreatomagmatic eruptions, and is generally consistent with SEM observations. Categorizing shards in this manner is only helpful after qualitative comprehensive SEM work is done to understand the significance of the quantitative assessment of shard values.

5) Extended time periods of homogenous magmatism from a single volcanic source are not uncommon and can be found in a variety of different tectonic settings. Nevertheless, Mt. Erebus is unique in exhibiting exceptionally homogenous major and trace element compositions across several types of eruptive products, including lava flows, volcanic bombs and ash.

6) The similar chemical composition of the glass from englacial tephra and historic bombs means that anorthoclase feldspar has crystallized to a similar degree out of the bulk magma during this time. Quenched glass is a screen shot of what the magma conditions were at the time of the eruption. In order for the major and trace elements to be consistent over large periods of time

(100’s to 1000’s of years), a stable magma chamber is required. Two possible mechanisms could produce consistent major and trace element chemistry: a) the magma chamber is composed of several batches of melt that evolve and fractionate to the same degree to produce this constant phonolite composition and any new batches readily equilibrate with the magma chamber, b) there is a single large magma body at depth that is in equilibrium and cannot differentiate any further because it is stuck in a thermal divide. The former is more likely because a parental basanite needs to be emplaced at depth to account for the constant high levels of CO_2 and magmatic water being degassed from the lava lake.

7) Tephra layers from the summit of Mt. Terra Nova exhibit a range of chemical compositions. One layer (EIT-003) a trachybasalt is likely erupted from a volcano near the Royal Society Range in the Erebus volcanic providence. EIT-007 is a trachytic tephra that has been correlated to a tephra erupted from Mt. Berlin in Marie Byrd Land ~1400km away. This layer is also correlated to a 28.5ka tephra in the Siple Dome ice core (SDMA-5683) and one in the WAIS divide core. This tephra layer is a possible link between West and East Antarctic ice cores and therefore, climate records.

Acknowledgements

Funding for this project was provided by the NSF Division of Polar Programs through Grant ANT- 0838817and ANT-1142083. Thanks to Matt Zimmerer, Dave Parmelee, Meghan Seifert, Laura Jones and everyone in G-081 for their assistance in the field. Field work was supported by Raytheon Polar Services Company. Great thanks to PHI, Inc. and Rob with Helicopters New

Zealand for their invaluable transportation to and from the field. Thanks to everyone in the NMGRL for assistance with ^{40}Ar/^{39}Ar dating.

References

Alloway, B. V., Larsen G., Lowe D.J., Shane, P.A.R., Westgate, J.A., 2006. Tephrochronology. Encyclopedia of Quaternary Science. 2869-2898.

Bintanja, R., 1999. On the glaciological, meteorological, and climatologically significance of Antarctic blue ice areas. Reviews of Geophysics 37(3): 337-359.

Buttner, R., Dellino, P., and Zimanowski, B., 1999. Identifying magma-water interaction from the surface features of ash particles: Nature, v. 401, no. 6754, p. 688-690.

Buttner, R., P. Dellino, L. La Volpe, V. Lorenz, and B. Zimanowski, 2002. Thermohydraulic explosions in phreatomagmatic eruptions as evidenced by the comparison between pyroclasts and products from Molten Fuel Coolant Interaction experiments, J. Geophys. Res. 107(B11), 2277.

Caldwell, D.A., Kyle, P.R., 1994. Minerology and geochemistry of ejecta erupted from Mt. Erebus, Antarctica, between 1972 and 1986. In: Kyle, P.R (Ed). Volcanology and Environmental Studies of Mt. Erebus, Antarctica, Antarctic Research Series, vol. 66. American Geophysical Union, Washington DC, pp. 147-162.

Calkins, J., Oppenheimer, C., Kyle, P.R., 2008. Ground-based thermal imaging of lava lakes at Erebus volcano, Antarctica. J. Volcanol. Geotherm. Res. 177, 695–704.

Cas, R.A.F., Wright, J.V., 1987. Volcanic successions, modern and ancient. Allen and Unwin, London, 527 pp.

Cashman, K.V., 1992. Groundmass crystallization of Mount St. Helens dacite, 1980–1986: a tool for interpreting shallow magmatic processes. Contrib. Mineral. Petrol. 109, 431– 449.

Clarke, H., Troll, V. R., and Carracedo, J. C., 2009. Phreatomagmatic to Strombolian eruptive activity of basaltic cinder cones: Montana Los Erales, Tenerife, Canary Islands: Journal of Volcanology and Geothermal Research, v. 180, no. 2-4, p. 225-245.

Corr, H.F.J., Vaughan, D.G., 2008. A recent volcanic eruption beneath the West Antarctic ice sheet. Nature Geoscience **1**, 122 – 125

Davidson, J., Hassanzadeh, J., Berzins, R., Stockli, D.F., Bashukooh, B., Turrin, B., Pandamouz, A., 2004. The geology of Damavand volcano, Alborz Mountains, northern Iran. Geological Society of America Bulletin 116, 16–29.

Dellino, P., La Volpe, L., 1996. Image processing analysis in reconstructing fragmentation and transportation mechanisms of pyroclastic deposits. The case of Monte Pilato–Rocche Rosse eruptions, Lipari Islands (Aeolian Islands, Italy). J. Volcanol. Geotherm. Res. 71, 13–29.

Dellino, P., Gundmundsson, M.T., Larsen, G., Mele, D., Stevenson, J.A., Thordarson, T., Zimanowski, B., 2012. Ash from the Eyjafjallajokull eruption (Iceland): Fragmentation processes and aerodynamic behavior. Journal of Geophysical Research, 117.

Doubik P., Hill B.E., (1999) Magmatic and hydromagmatic conduit development during the 1975 Tolbachik Eruption, Kamchatka, with implications for hazards assessment at Yucca Mountain, NV. J Volcanol Geotherm Res 91:43–64.

Dogan A.U., Dogan, M., Peate, D.W., Dogruel, Z., 2011. Textural and mineralogical diversity of compositionally homogeneous dacites from the summit of Mt. Erciyes, Central Anatolia, Turkey. Lithos, volume 127, issues 3–4, pages 387–400.

Dunbar, N.W., Cashman, K.V., Dupre, R., 1994. Crystallization processes of anorthoclase phenocrysts in the Mount Erebus magmatic system: evidence from crystal composition, crystal size distributions, and volatile contents of melt inclusions. In: Kyle, P.R (Ed). Volcanology and Environmental Studies of Mt. Erebus, Antarctica, Antarctic Research Series, vol. 66. American Geophysical Union, Washington DC, pp. 129-146.

Dunbar, N. W., Zielinski, G.A. and Voisins, D.T., 2003. Tephra layers in the Siple Dome and Taylor Dome ice cores, Antarctica: Sources and correlations. Journal of Geophysical Research, v. 108, no. B8.

Dunbar, N. W., McIntosh, W. C., and Esser, R. P., 2008. Physical setting and tephrochronology of the summit caldera ice record at Mount Moulton, West Antarctica. Geological Society of America Bulletin, v. 120, no. 7-8, p. 796-812.

Dunbar, N. W., and Kurbatov, A. V., 2011. Tephrochronology of the Siple Dome ice core, West Antarctica: correlations and sources. Quaternary Science Reviews, v. 30, no. 13-14, p. 1602-1614.

Durig, T, Mele, D., Dellino, P., and Zimanowski, B., 2012. Comparative analysis of glass fragments from brittle fracture experiments and volcanic ash particles. Bulletin of Volcanology 74, 691-704.

Esser, R. P., McIntosh, W. C., Heizler, M.T. and Kyle, P.R., 1997. Excess argon in melt inclusions in zero-age anorthoclase feldspar from Mt. Erebus, Antarctica, as revealed by the Ar-40/Ar-39 method. Geochimica Et Cosmochimica Acta 61(18): 3789-3801.

Esser, R.P. and Kyle, P.R. 2002. ^{40}Ar/^{39}Ar chronology of the McMurdo Volcanic Group at The Pleiades, northern Victoria Land, Antarctica. In Antarctica at the close of a Millenium (ed D. Skinner) Proceedings of the 8th International Symposium on Antarctic Earth Sciences, Royal Society of New Zealand Bulletin 35, Wellington. p. 415-418

Esser, R. P., Kyle, P. R., and McIntosh, W. C., 2004. 40Ar/39Ar dating of the eruptive history of Mount Erebus, Antarctica: volcano evolution. Bulletin of Volcanology, v. 66, no. 8, p. 671-686.

Gow, A., Meese, D.A., 2005. The distribution and timing of tephra deposition at Siple Dome, Antarctica: possible climatic and rheologic implications. Journal of Glaciology 53 (183), 585-596

Harpel, C. J., Kyle, P. R., Esser, R. P., McIntosh, W. C., and Caldwell, D. A., 2004. 40Ar/39Ar dating of the eruptive history of Mount Erebus, Antarctica: summit flows, tephra, and caldera collapse. Bulletin of Volcanology, v. 66, no. 8, p. 687-702.

Harpel, C. J., Kyle, P. R., and Dunbar, N. W., 2008. Englacial tephrostratigraphy of Erebus volcano, Antarctica. Journal of Volcanology and Geothermal Research, v. 177, no. 3, p. 549-568.

Heiken, G., Wohletz, K., 1985. Volcanic Ash. University of California Press, Berkeley.

Hillenbrand, C. D., Moreton, S. G., Caburlotto, A., Pudsey, C. J., Lucchi, R. G., Smellie, J. L., Benetti, S., Grobe, H., Hunt, J. B., and Larter, R. D., 2008. Volcanic time-markers for Marine Isotopic Stages 6 and 5 in Southern Ocean sediments and Antarctic ice cores: implications for tephra correlations between palaeoclimatic records: Quaternary Science Reviews, v. 27, no. 5-6, p. 518-540.

Inman, D.L., 1952. Measures for describing the size distribution of sediments. Journal of Sedimentary Petrology, v. 22, p. 125–145.

Kelly, P. J., Dunbar, N. W., Kyle, P. R., and McIntosh, W. C., 2008a. Refinement of the late Quaternary geologic history of Erebus volcano, Antarctica using 40Ar/39Ar and 36Cl age determinations. Journal of Volcanology and Geothermal Research, v. 177, no. 3, p. 569-577.

Kelly, P. J., Kyle, P. R., Dunbar, N. W., and Sims, K. W. W., 2008b. Geochemistry and mineralogy of the phonolite lava lake, Erebus volcano, Antarctica: 1972–2004 and comparison with older lavas. Journal of Volcanology and Geothermal Research, v. 177, no. 3, p. 589-605.

Keys, J. R., Anderton, P. W., and Kyle, P. R., 1977. Tephra and Debris layers in Skelton Neve and Kempe Glacier, South Victoria Land, Antarctica. New Zealand Journal of Geology and Geophysics, v. 20, no. 5, p. 971-1002.

Knox, H.A., 2012. Eruptive Characteristics and Glacial Earthquakes Investigation on Erebus Volcano, Antarctica PhD Dissertation, New Mexico Tech.

Kyle, P. R., 1977. Mineralogy and Glass chemistry of recent volcanic ejecta from Mt. Erebus, Ross Island, Antarctica. New Zealand Journal of Geology and Geophysics 20(6): 1123-1146.

Kyle, P.R, 1982. Volcanic geology of The Pleiades, northern Victoria Land, Antarctica, in Antarctic Geoscience, edited by C. Craddock, pp. 747-754, University of Wisconsin Press, Madison.

Kyle, P., Dibble, R., Giggenbach, W., Keys, J., 1982. Volcanic activity associated with the anorthoclase phonolite lava lake, Mt. Erebus, Antarctica. In: Craddock, C. (Ed.), Antarctic Geosciences. Univ. Wisc. Press, Madison, pp. 735–745.

Kyle, P.R., 1990a. McMurdo Volcanic Group Western Ross Embayment: Introduction In: "Volcanism of the Antarctic Plate and Southern Oceans" (Ed. W. LeMasurier, J. Thompson). Antarctic Research Series, Vol. 48, American Geophysical Union, 18-25.

Kyle, P.R., 1990b. Erebus volcanic Province: Summary. In: "Volcanism of the Antarctic Plate and Southern Oceans" (Ed. W. LeMasurier, J. Thompson). Antarctic Research Series, Vol. 48., American Geophysical Union, 81-88.

Kyle, P.R., 1990c. Melbourne volcanic Province: Summary. In: "Volcanism of the Antarctic Plate and Southern Oceans" (Ed. W. LeMasurier, J. Thompson). Antarctic Research Series, Vol. 48, American Geophysical Union, 48-52.

Kyle, P.R., Moore, J.A., Thirlwall, M.F., 1992. Petrologic evolution of anorthoclase phonolite lavas at Mount Erebus, Ross Island, Antarctica. Journal of Petrology 33 (4), 849–875.
.LeBas, M.J., LeMaitre, R.W., Streckeisen, A., Zanettin, B., 1986. A chemical classification of volcanic rocks based on the total alkali silica diagram. J. Petrol. 27, 745–750.

Lautze, N. C., Taddeucci, J., Andronico, D., Cannata, C., Tornetta, L., Scarlato, P., Houghton, B., Lo Castro, M.D., 2012. SEM-based methods for the analysis of basaltic ash from weak explosive activity at Etna in 2006 and the 2007 eruptive crisis at Stromboli. Physics and Chemistry of the Earth 45-46, 113-127.

LeMasurier, W., Thomson, J., 1990. Volcanism of the Antarctic Plate and the southern ocean, Antarctic Research Series, vol. 48. American Geophysical Union.

Lowe, D. J., 2011, Tephrochronology and its application: A review: Quaternary Geochronology, v. 6, no. 2, p. 107-153.

Marske, J. P., M. O. Garcia, A. J. Pietruszka, J. M. Rhodes, and M. D. Norman, 2008. Geochemical variations during Kilauea's Pu'u 'O'o eruption reveal a fine-scale mixture of mantle heterogeneities within the Hawaiian mantle plume. J. Petrol., 49, 1297–1318.

Martin, A.P.; Cooper, A.F.; Dunlap, W.J. 2010 Geochronology of Mount Morning, Antarctica: two-phase evolution of a long-lived trachyte-basanite-phonolite eruptive center. Bulletin of Volcanology, 72(3): 357-371.

Moore, J.A., Kyle, P.R., 1987. Volcanic geology of Mt. Erebus, Ross Island, Antarctica. Proceeding of the NIPR Symposium on Antarctic Geosciences vol. 1, Tokyo, Japan, pp. 48-65.

Narcisi, B., Petit, J. R., Delmonte, B., Scarchilli, C., and Stenni, B., 2012. A 16,000-yr tephra framework for the Antarctic ice sheet: a contribution from the new Talos Dome core. Quaternary Science Reviews, v. 49, no. 0, p. 52-63.

Nemeth, K., 2010, Volcanic glass textures, shape characteristics and compositions of phreatomagmatic rock units from the Western Hungarian monogenetic volcanic fields and their implication for magma fragmentation. Central European Journal of Geosciences, 2(3), 399-419.

Oppenheimer, C., Kyle P. (editors). 2008. Volcanology of Erebus volcano, Antarctica. Journal of Volcanology and Geothermal Research 177.

Oppenheimer, C., Kyle, P., 2008. Probing the magma plumbing of Erebus volcano, Antarctica, by open-path FTIR spectroscopy of gas emissions. J. Volcanol. Geotherm. Res. 177, 743–754.

Palais, J.M., Kyle, P.R., McIntosh, W.C., Seward, D., 1988. Magmatic and phreatomagmatic volcanic activity at Mt. Takahe, West Antarctica based on tephra layers in the Byrd ice core and field observations at Mt. Takahe. J. Volcanol. Geotherm. Res., 35, 295-317.

Panter, K.S., and Winter, B., 2008. Geology of the Side Crater of the Erebus volcano, Antarctica. Journal of Volcanology and Geothermal Research 177, 578-588.

Paulsen, T.S., Wilson, T.J., 2009. Structure and age of volcanic fissures on Mount Morning: A new constraint on Neogene to contemporary stress in the West Antarctic Rift, southern Victoria Land, Antarctica. Geological Society of America Bulletin, 121, no. 7-8; 1071-1088.

Pearce, N. J. G., Perkins, W. T., Westgate, J. A., Gorton, M. P., Jackson, S. E., Neal, C. R., and Chenery, S. P. (1997). A compilation of new and published major and trace element data for NIST SRM 610 and NIST SRM 612 glass reference materials. *Geostandards Newsletter* 21, 115-144.

Pearce, N. J. G., Perkins, W. T., Westgate, J. A., and Wade, S. C., 2011. Trace-element microanalysis by LA-ICP-MS: The quest for comprehensive chemical characterisation of single, sub-10 mu m volcanic glass shards. Quaternary International, v. 246, p. 57-81.Ross, J. 1847: "Voyage to the Southern Seas". Vol. I. John Murray, London.

Renne, P.R., Swisher, C.C., Deino, A.L., Karner, D.B., Owens, T.L., Depaolo, D.J., 1998. Intercalibrations of standards, absolute ages and uncertainties in 40Ar/39Ar dating. Chemical Geology, 145 (1-2): 117-152.

Ross, J. 1847: "Voyage to the Southern Seas". Vol. I. John Murray, London.

Ross, J.I., McIntosh, W.C., Dunbar N.W., 2012. Development of a precise and accurate age–depth model based on ^{40}Ar/^{39}Ar dating of volcanic material in the ANDRILL (1B) drill core, Southern McMurdo Sound. Antarctica Global and Planetary Change, Volumes 96–97, October–November 2012, Pages 118–130.

Rowe, C. A., Aster, R. C., Kyle, P. R., Dibble, R. R., Schlue, J. W., 2000. Seismic and acoustic observations at Mount Erebus Volcano, Ross Island, Antarctica, 1994-1998. Journal of Volcanology and Geothermal Research 101(1-2): 105-128.

Sheridan, M. F. and J. R. Marshall, 1983. Interpretation of pyroclast surface features using SEM images. Journal of Volcanology and Geothermal Research. 16, 153-159.

Sheridan, M. F., K. H. Wohletz, et al., 1987. Discrimination of grain size subpopulation in pyroclastic deposits. Geology 15(4): 367-370.

Sims, K.W.W., Blichert-Toft, J., Kyle, P.R., Pichat, S., Bluzstajn, J., Kelly, P., Ball, L., Layne, G., 2008. A Sr, Nd, Hf, and Pb isotope perspective on the genesis and long-term evolution of alkaline magmas from Erebus volcano, Antarctica. Journal of Volcanology and Geothermal Research 177, 606-618.

Streck, M. J., Dungan, M. A., Bussy, F., and Malavassi, E., 2005. Mineral inventory of continuously erupting basaltic andesites at Arenal volcano, Costa Rica: implications for interpreting monotonous, crystal-rich, mafic arc stratigraphies. Journal of Volcanology and Geothermal Research, v. 140, no. 1-3, p. 133-155.

Sumner, C.L.K., 2007. Residence time estimates and controls on crystallization patterns for anorthoclase phenocrysts in phonolite magma, Erebus volcano, Antarctica. MS Thesis, New Mexico Tech

Taylor, K. C., Alley, R. B., Meese, D. A., Spencer, M. K., Brook, E. J., Dunbar, N. W., Finkel, R. C., Gow, A. J., Kurbatov, A. V., Lamorey, G. W., Mayewski, P. A., Meyerson, E. A., Nishiizumi, K., and Zielinski, G. A., 2004, Dating the Siple Dome (Antarctica) ice core by manual and computer interpretation of annual layering: Journal of Glaciology, v. 50, no. 170, p. 453-461.

Thorarinsson, S., 1944. Tefrokronologiska studier pa island (Tephrochronological studies in Iceland). Geografiska Annaler 1-2, 1-217.

Thorarinsson, S., 1966. Surtsey: The New Island in the North Atlantic, Reykjavik, Almenna Bokafelagio.

Walker, G.P.L., 1971. Grain-size characteristics of pyroclastic deposits. Journal of Geology, v. 79, p. 696–714.

Walker, G.P.L., and Crosdale, R., 1972, Characteristics of some basaltic pyroclastics: Bulletin of Volcanology, v. 35, p. 303–317.

Wohletz, K. H., 1983. Mechanism of hydrovolcanic pyroclasts formation: Grain size, scanning electron microscopy, and experimental studies. Journal of Volcanology and Geothermal Research, v. 17, no. 1-4, p. 31-63.

Worner, G., H. Niephaus, J. Hertogen, and L. Viereck, 1989. The Mt. Melbourne volcanic field(Victoria Land, Antarctica), II, Geochemistry and magmagenenesis, Geol. Jahrb.

Wong, L.J., Larsen, J.F., 2010. The Middle Scoria sequence: a Holocene violent Strombolian, subplinian and phreatomagmatic eruption of Okmok volcano, Alaska. Bulletin of Volcanology 72, 17–31.

Zimanowski, B., Buttner, R., Lorenz, R., Hafele H.G., 1997. Fragmentation of basaltic melt in the course of explosive volcanism. Journal of Geophysical Research, Vol. 102, no. B1, pages 803-814.

Zimanowski, B., Wohletz, K., Dellino, P., and Buttner, R., 2003. The volcanic ash problem. Journal of Volcanology and Geothermal Research, v. 122, no. 1-2, p. 1-5.

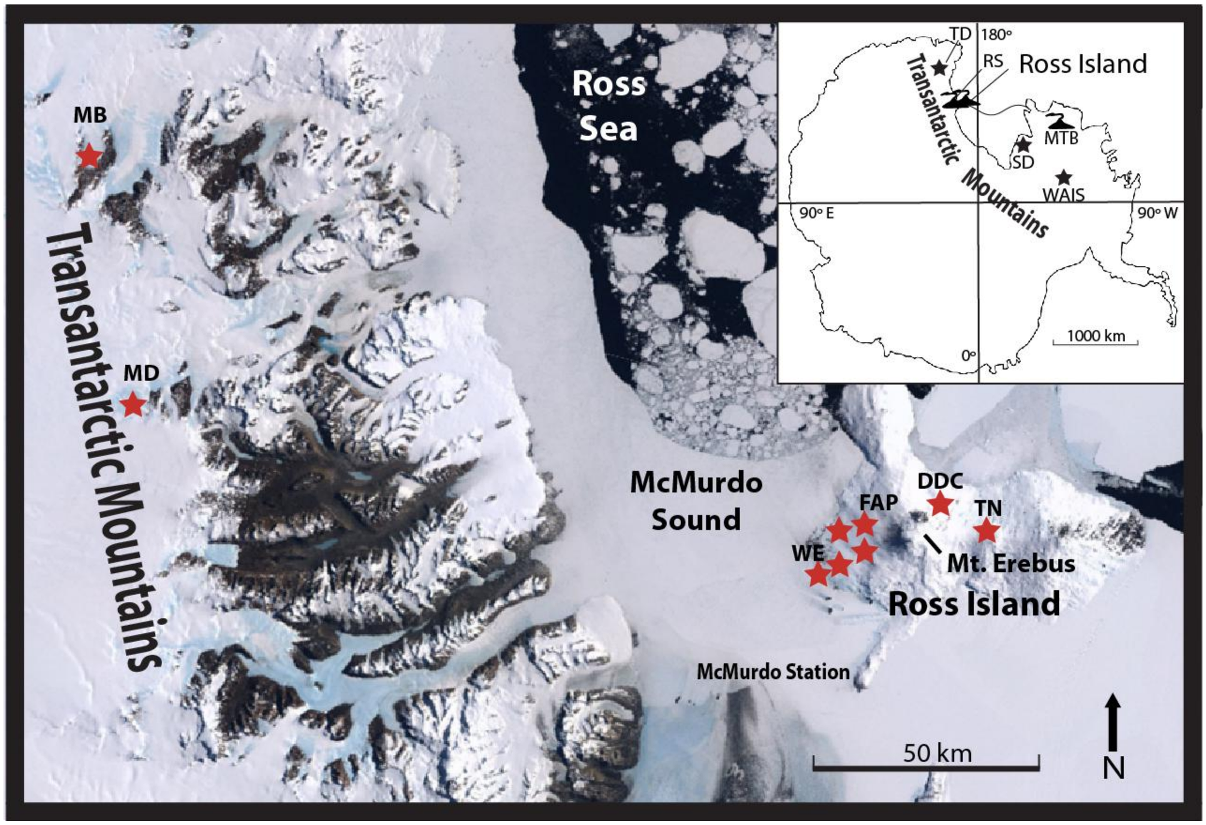

Fig. 1 Location of tephra samples from Ross Island and the Transantarctic Mountains. Stars represent blue ice areas where samples were collected. MB= Manhaul Bay, MD= Mt. DeWitt, TN= Terra Nova, DDC=”Dead Dinosaur Cone”, FAP=”False Abbot Peak” and WE= West Erebus. The 4 West Erebus samples are individual sample locations that have no visible stratigraphy. Inset- black stars represent ice cores: TD=Talos Dome ice core, SD = Siple Dome ice core and WAIS= West Antarctic Ice Sheet Divide ice core. Black volcanoes represent tephra source: Ross Island (Mt. Erebus), RS= Royal Society Range and MTB= Mt. Berlin. MB and MD (Harpel et al., 2008), and TD (Narcissi et al., 2012) are Erebus distal tephra sites.

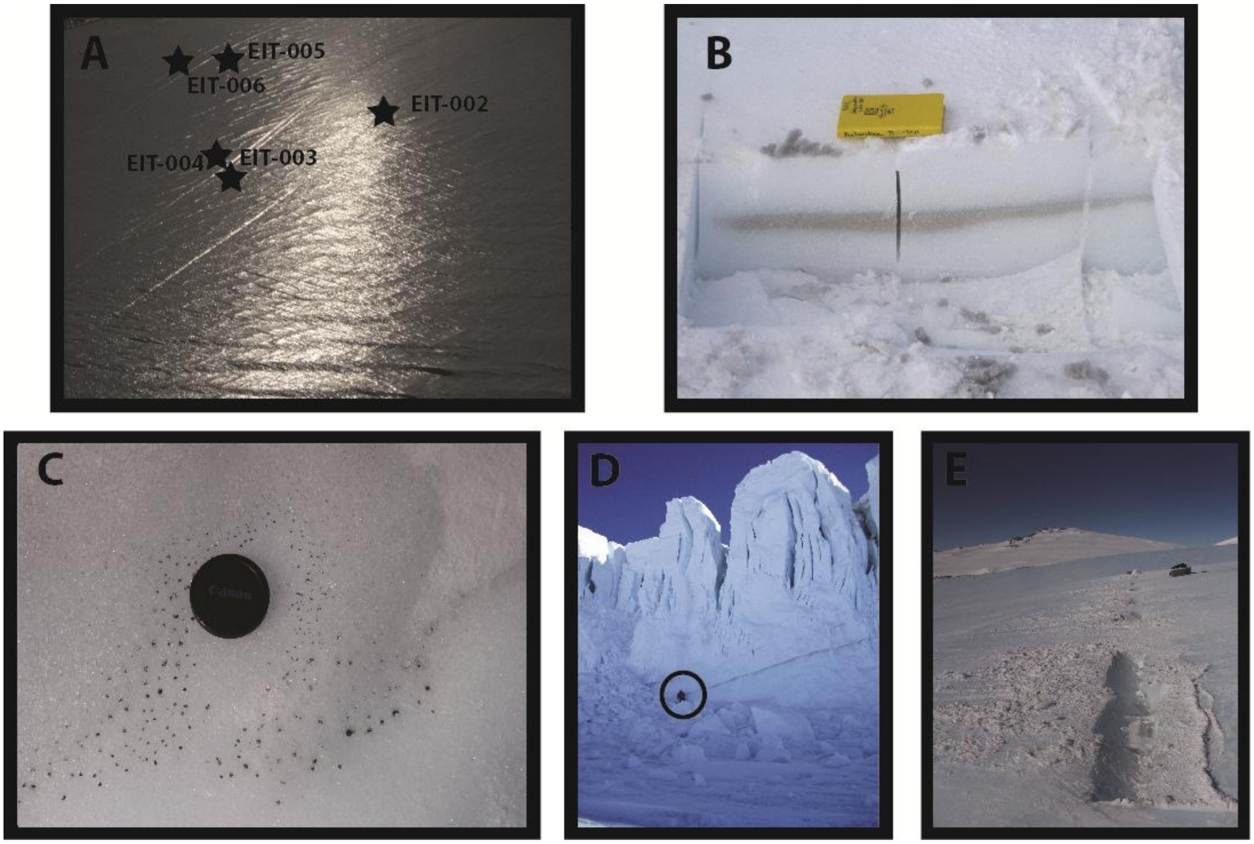

Fig. 2 Photos of tephra layers. A) Five tephra layers on Terra Nova Summit Glacier. Tephra layers are only visible as depressions in the ice due to melting induced by the dark tephra particles. Rightmost depression (EIT-002) is ~10cm wide. Tephra layers are labeled with black stars. The top of the section is sample EIT-002 and bottom of the section is EIT-006. B) Exposed tephra layer EIT-008 in a pit. Field book for scale (1.5cm thick, 19cm length). Layer is a concentrated lens 40cm in length and 2-4cm wide. Lenses like these are common and occur where a layer has been concentrated by aeolian processes. C) Melt pods in EIT-012 (lens cap is 5.5cm in width). Most pods are a few cm to <1cm wide. Shards are dark golden brown in color. D) EBT-1 (sampled by Harpel et al., 2008) at the terminus of the Barne Glacier. ~2m person circled for scale. E) Sampled EIT-006 at the Terra Nova Summit with Mt. Terror in background. Coolers for scale in the back, ~width of extraction pits is 50cm. Multiple blocks were extracted because of the extremely diffuse nature of the layer.

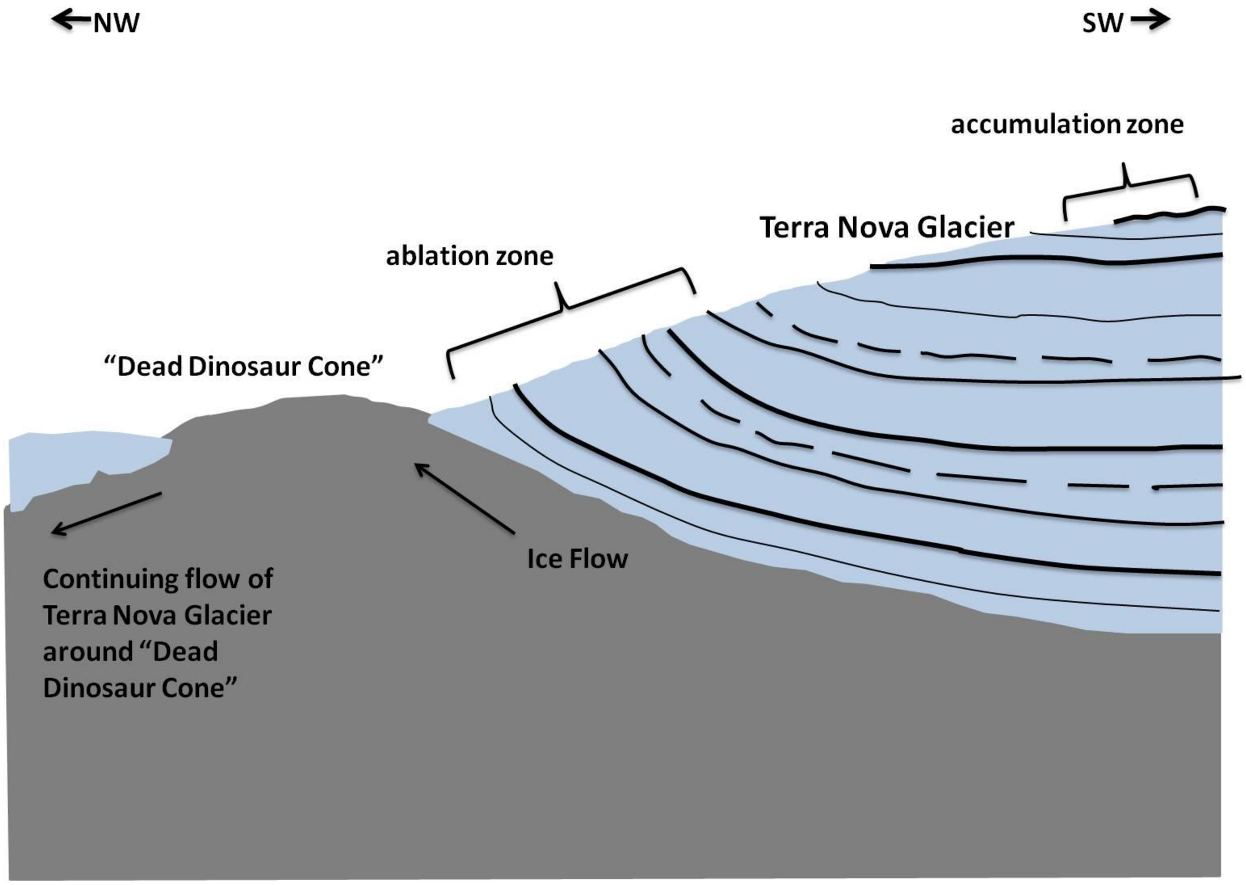

Fig. 3 Cartoon drawing of the transport of tephra and its entrainment in the Terra Nova glacier (not to scale). Accumulation zone is the location where tephra and snow accumulate and burial begins. Note that the tephra layers remain in stratigraphic order when they return to the surface; this is an important speculation. The cartoon is modified from Dunbar et al. (2008).

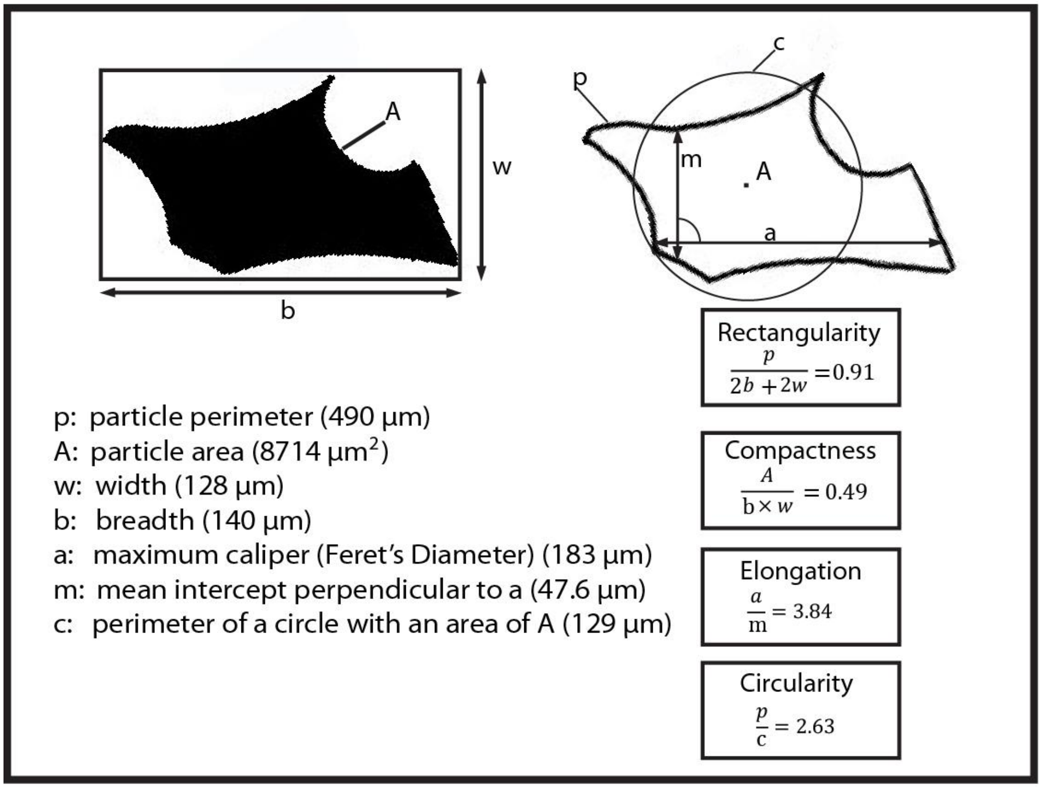

Fig. 4 Diagram of IPA parameters (after Durig et al 2012). The particle EIT-034-8 was chosen as an example and actual values are presented for the four parameters.

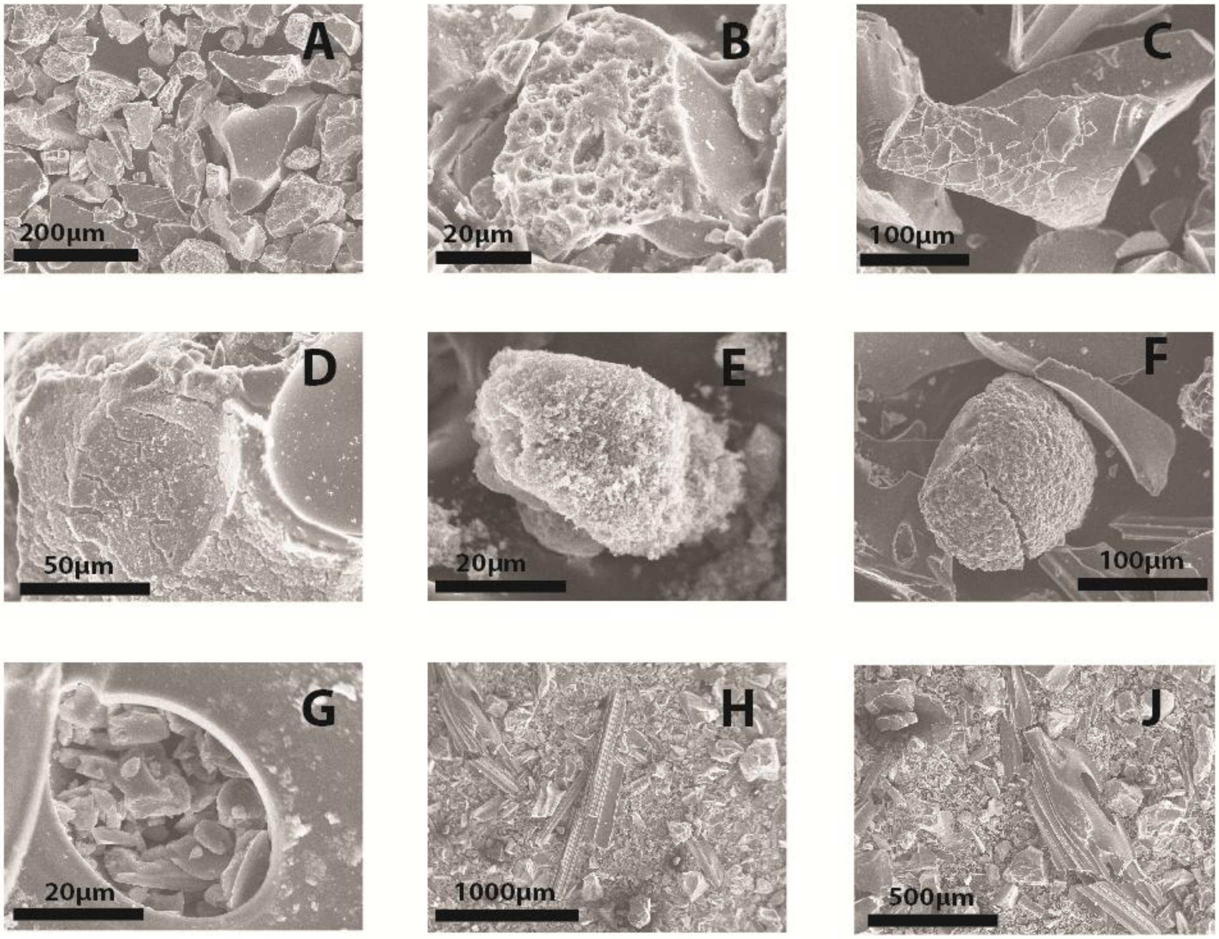

Fig. 5 SEM images of typical shard morphologies of phreatomagmatic tephra shards. A) Typical phreatomagmatic tephra with low vesicularity, blocky shape, and chipped margins; B) Shard with acid pitting; C) Turbulent shedding; D) Hydration rind with sublimates attached to the shard; E) Dust aggregate, made of very fine grained particles adhering together; F) Large quench fracture with sublimates; G) Vesicle filled with finer particles; H) Mixed ash with large elongated pumice and smaller block shards; J) Close up of fluidal shard mixed with fine particles.

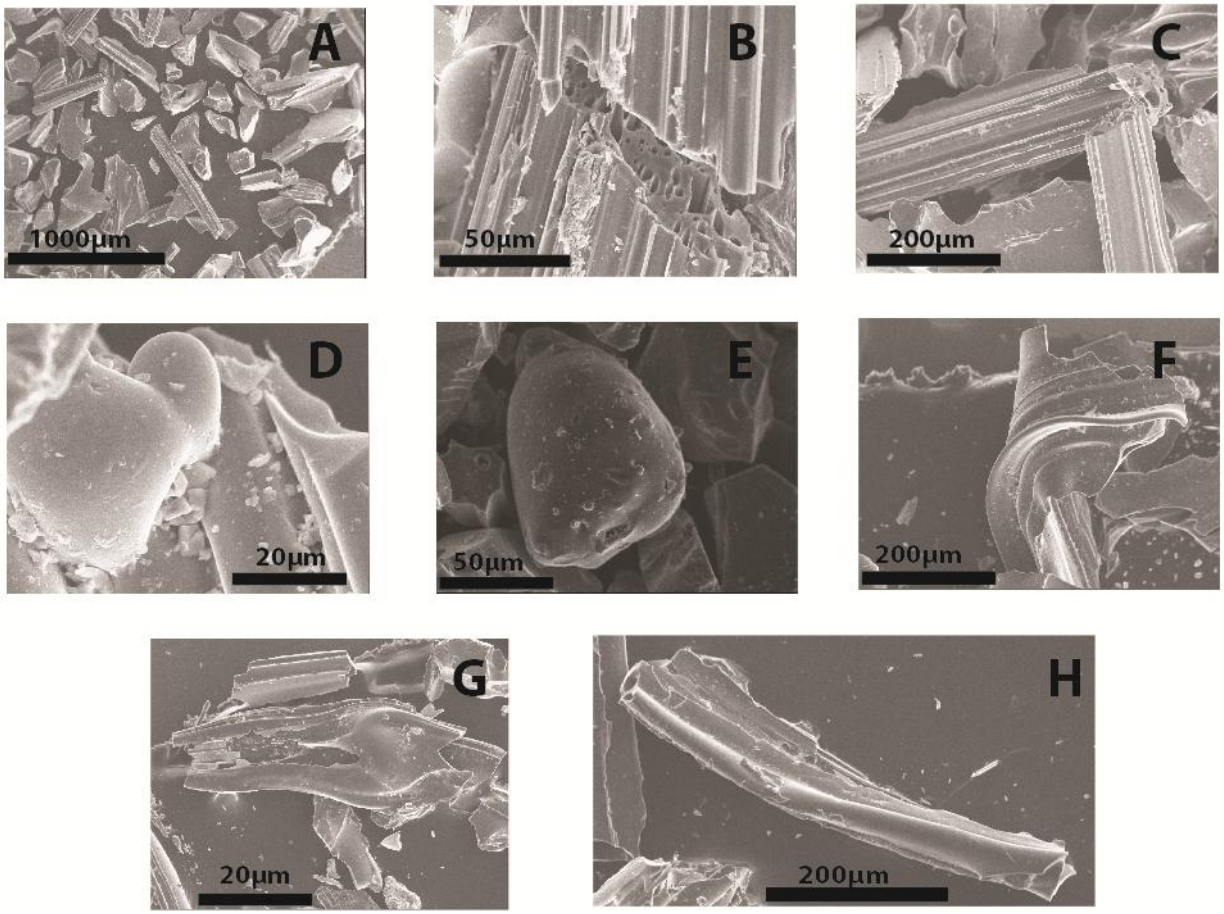

Fig. 6 SEM images of typical shard morphologies of magmatic tephra. A) Angular and elongated well vesiculated shards; B) Pele's hair with elongated vesicles; C) Elongated shard with numerous tubular vesicles; D) Ash budding, where two fluidal droplets were hot enough to agglutinate together; E) Large fluidal droplet with several smaller droplets budding; F) Fluidal shard, deformed plastically while shard was still hot; G) Broken Pele's hair with large fluidal bulb at the end; H) Typical Pele's hair.

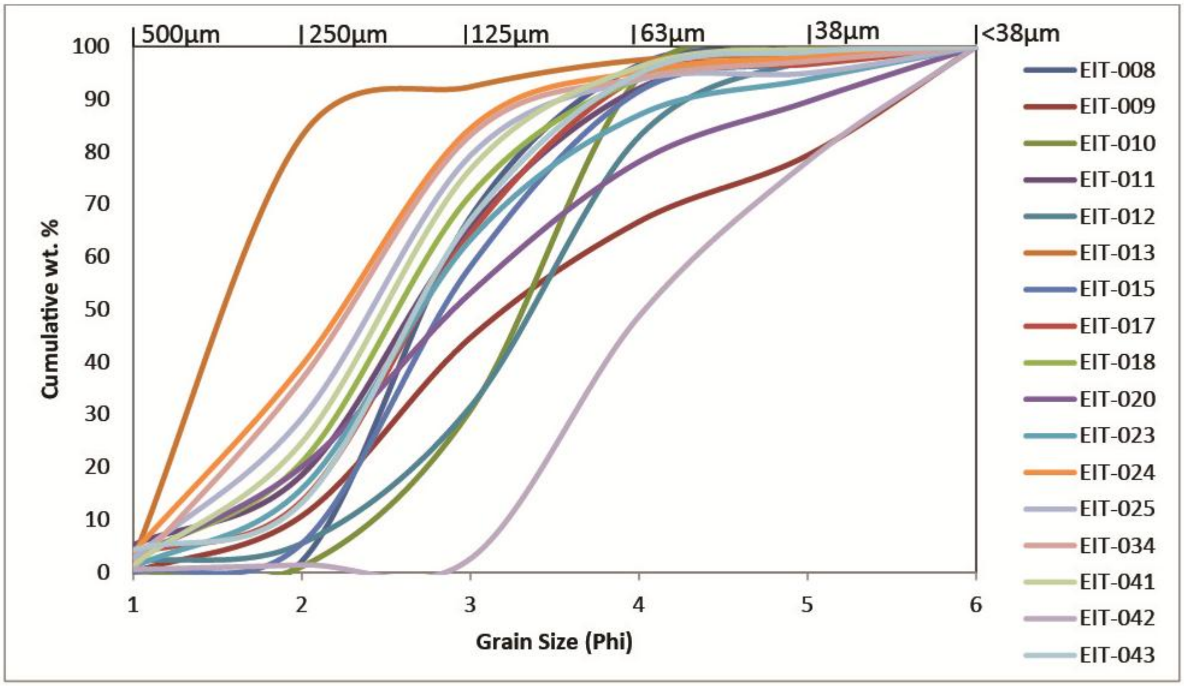

Fig. 7 Graphical representation of the cumulative wt. % grain size distribution for all of the tephra that was sufficiently abundant for grain size analysis.

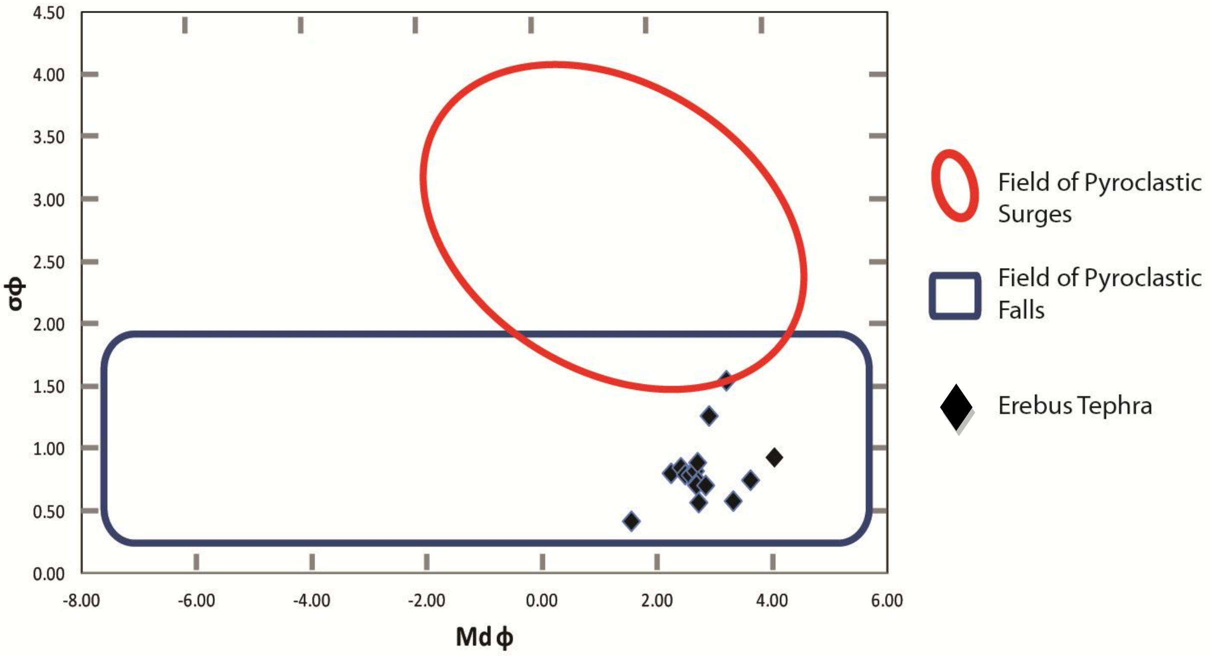

Fig. 8 Plot showing median diameter (Md) versus sorting (σ) in phi (ϕ) units for Erebus tephra. All Erebus tephra are well to very well sorted (Cas and Wright, 1987). The higher the σ_ϕ the more poorly sorted the tephra. The red and blue fields respectively indicate pyroclastic surge and fall deposit fields of Walker (1971). µ

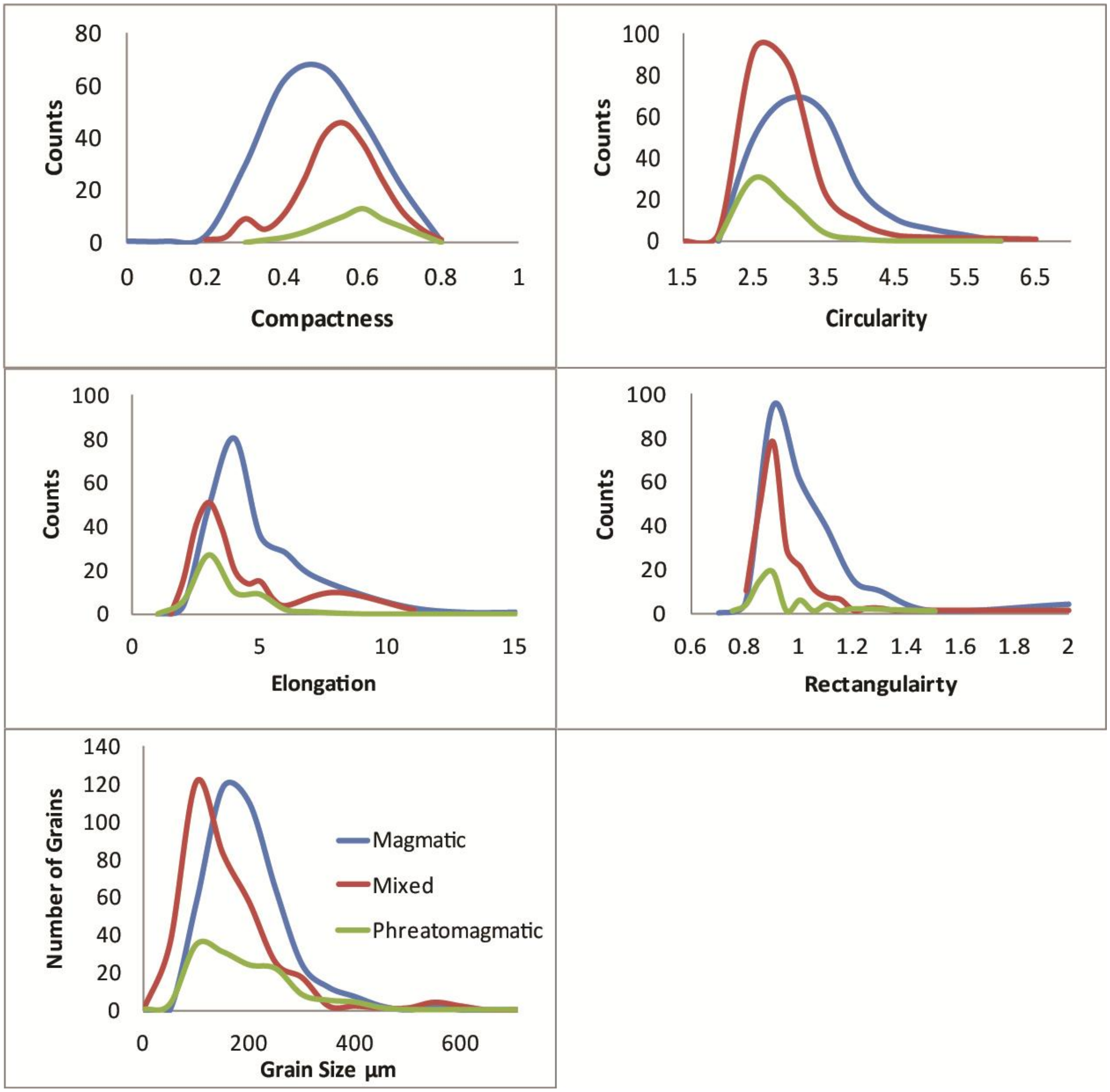

Fig. 9 Histograms of grain sizes of all samples analyzed by IPA. Graphical representation of IPA analyses based morphological characteristics determined by SEM imagery. IPA of magmatic layers are in blue, mixed layers are in red and phreatomagmatic are in green.

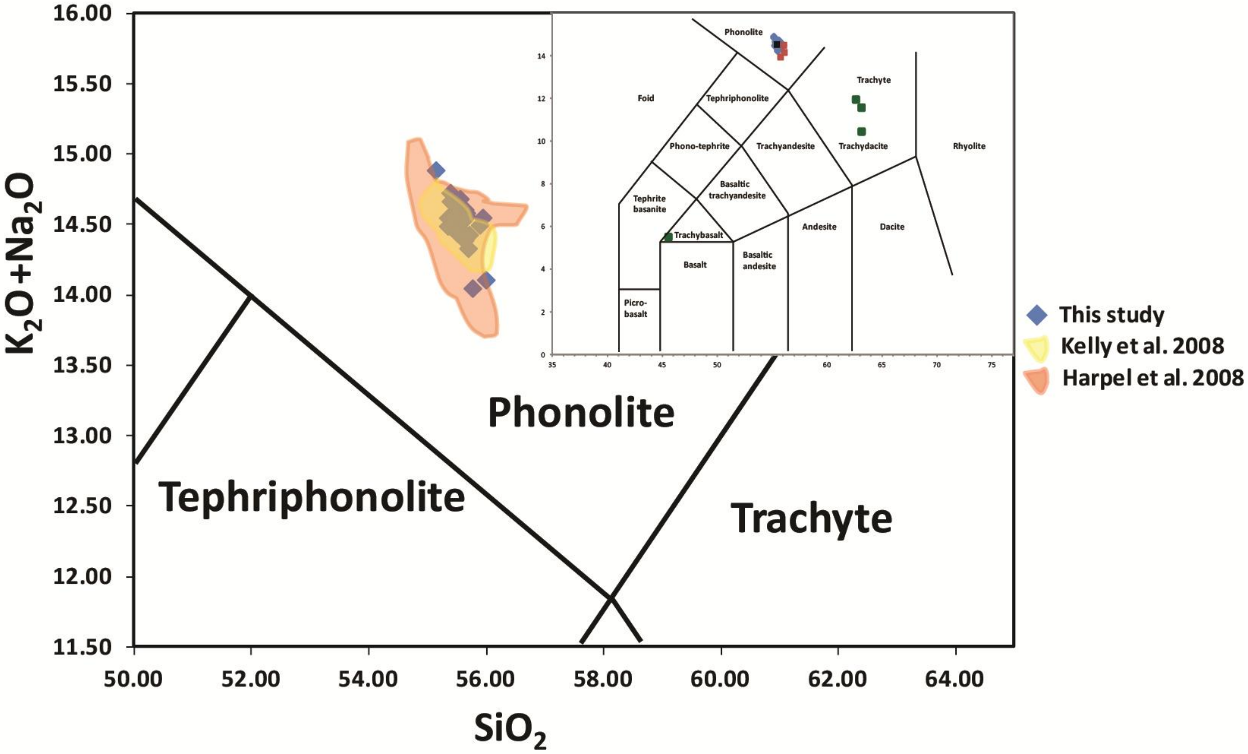

Fig. 10 Total alkalis versus silica (TAS) diagram after LaBas et al. (1986) of all glass analyses (inset Blue diamond= Erebus derived phonolites, Black square= distal tephra from Erebus, Red square= Erebus phonolites found at Terra Nova Summit, Green square =distal non-Erebus volcanic deposited at Terra Nova Summit.). The yellow area represents analyses of glass from volcanic bombs erupted from 1972-2005 (Kelly et al., 2008). The orange area shows compiled glass analysis of englacial tephra from the flanks of Erebus (Harpel et al., 2008). This study (blue diamonds) sampled different tephra than Harpel et al. (2008).

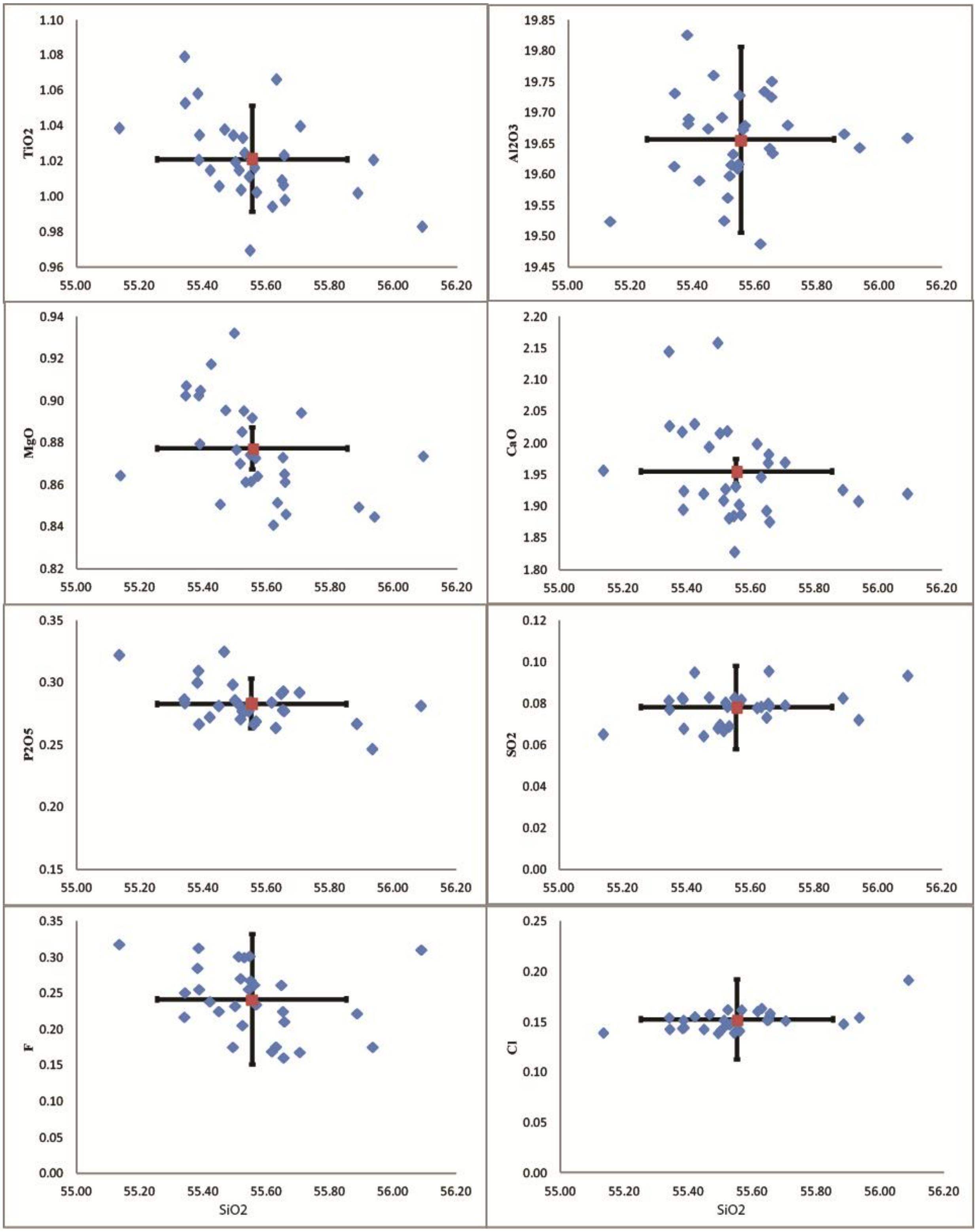

Fig. 11 Selected Harker diagrams of phonolite glass in tephra from the flanks of Erebus. Blue diamonds are averaged analyses of individual shards from a single tephra layers. Red square is the mean Erebus phonolite composition determined from averaging all tephra analyses. Error bars represent analytical precision determined by multiple analysis of a standard glass (KE12).

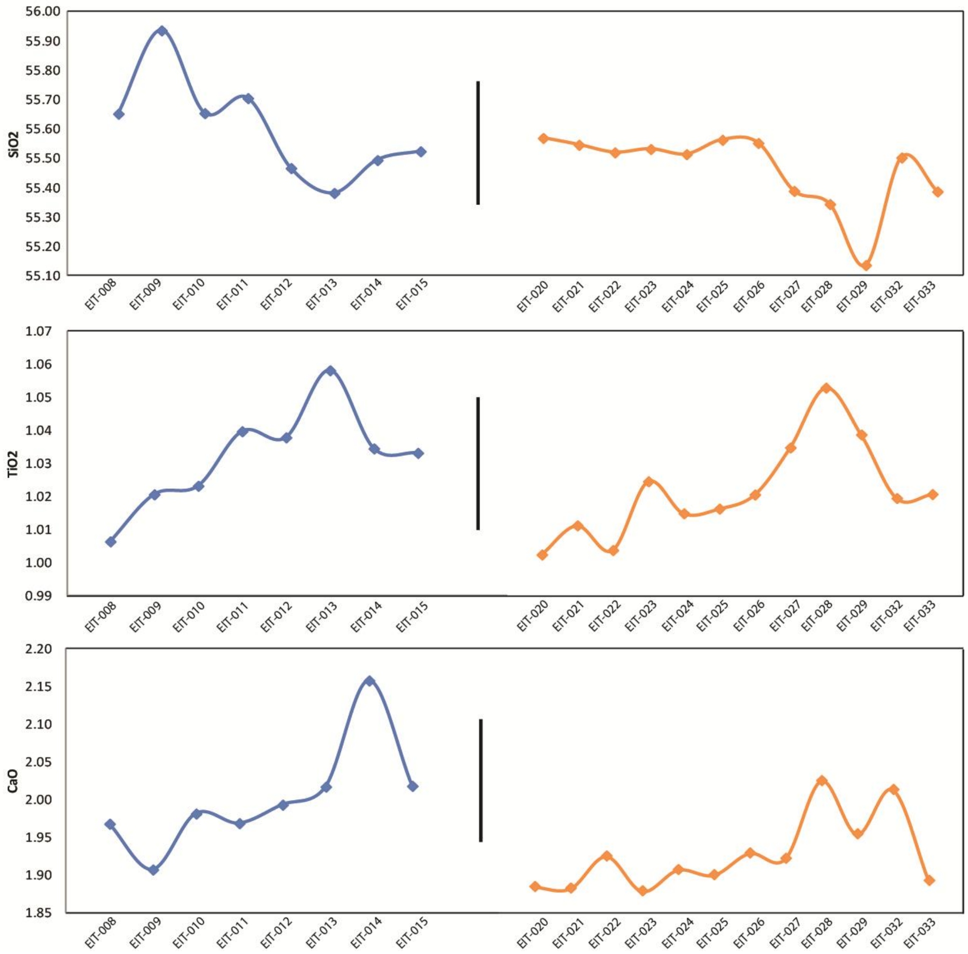

Fig. 12 Geochemical trends from "Dead Dinosaur Cone" (Blue) and "False Abbot Blue Ice" (Orange). The black bar represents one standard deviation in the data from all Erebus phonolites. Samples are listed from youngest (higher in the stratigraphic sequence) on the left and oldest on the right.

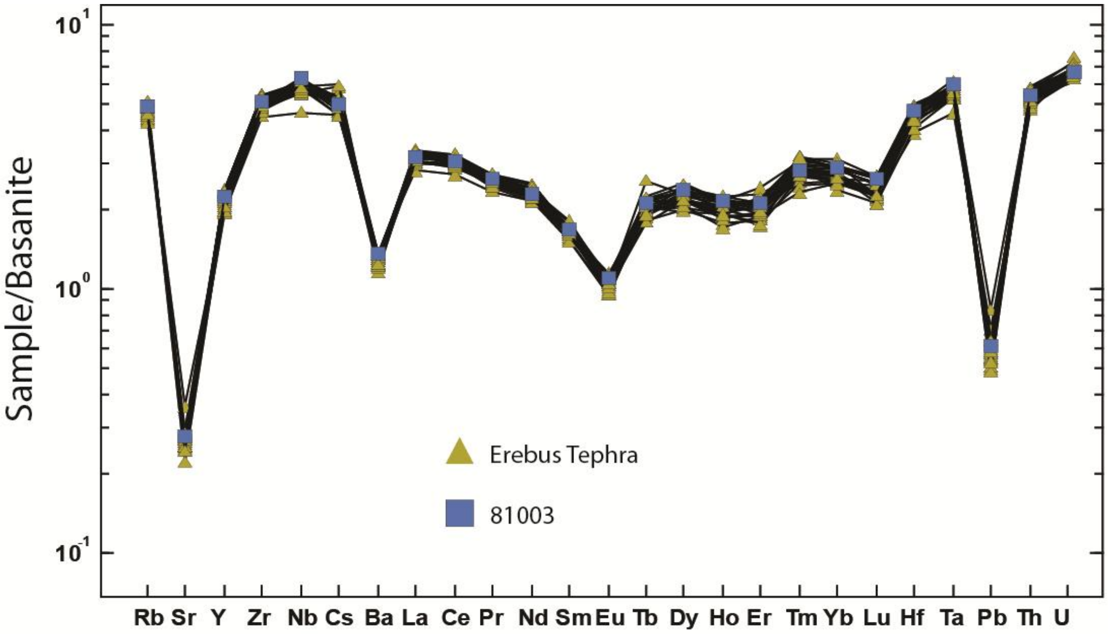

Fig. 13 Spider diagram of all Erebus tephra glass samples (N=23) normalized to a parental like basanite (EIT-003). 81003 (glass-sample from modern bomb) is added to show the homogeneity of trace elements at Erebus over the past ~30Ky. Errors are not shown but would be within the scatter of the data.

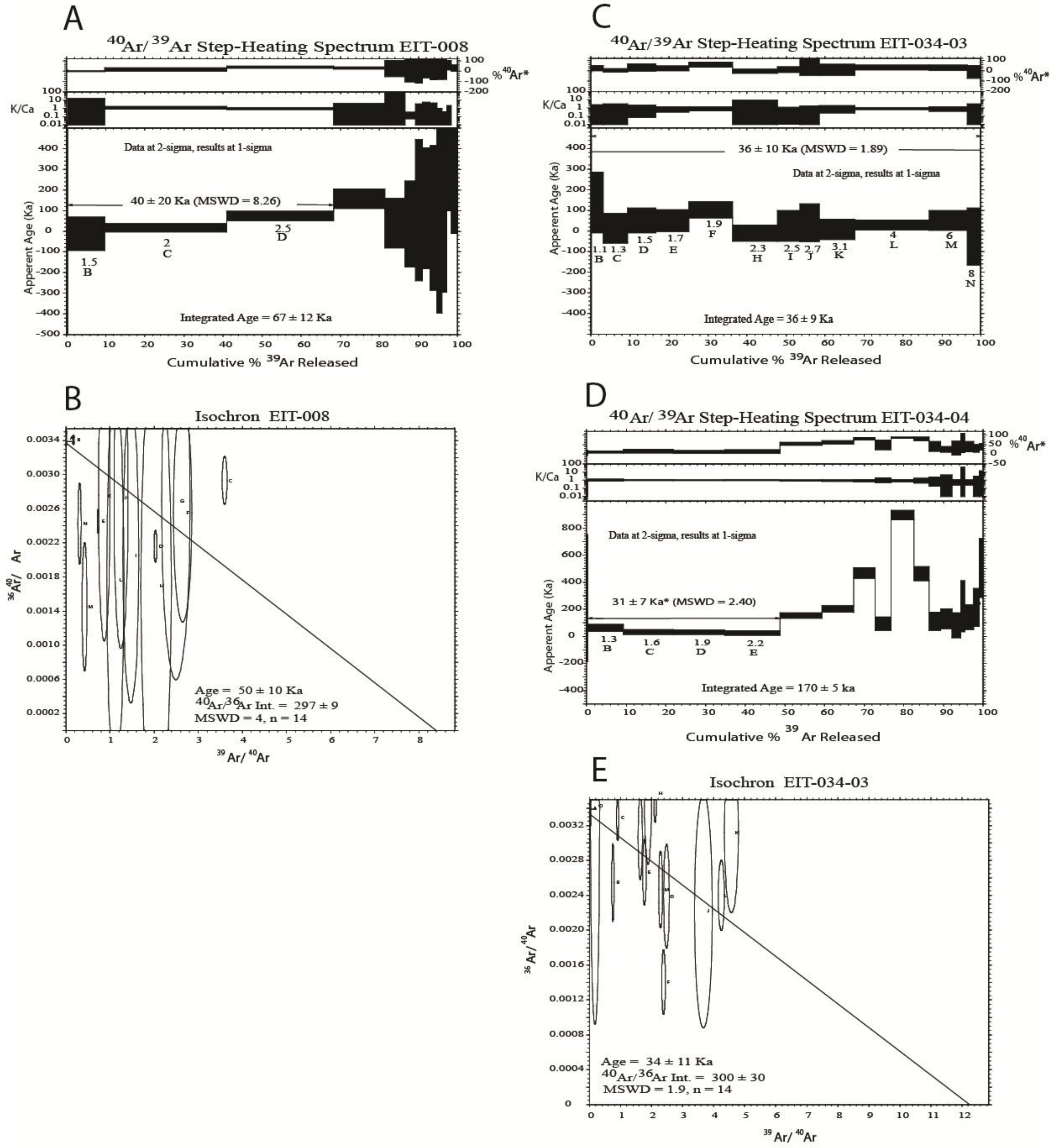

Fig. 14 Laser step heating ^{40}Ar/^{39}Ar age spectra (A, C, D) and inverse-isochrons (B and E) of englacial tephra from Erebus volcano. Weighted-mean ages are shown with error at 1σ. Each age spectra plot shows, from top to bottom, radiogenic yield of ^{40}Ar, K/Ca ratioand the apparent age. All plots are versus cumulative percent ^{39}Ar released on the X axis. Each step in the age spectra is an increase in wattage of the laser and no temperature is associated with each step. Precision of each step in the age spectra is at 2σ. Weighted-mean ages are calculated from at least 3 steps. Weighted-mean ages are shown with error at 1σ. Integrated ages are also. Large differences are from excess Ar being released at higher temperature. Inverse-isochrons (B and E) are used to show if excess Argon is present. It is difficult to interpret excess Ar because of the large errors associated with each measurement. The inverse isochrons show no excess Ar, which is not consistent with observations from the age spectra.

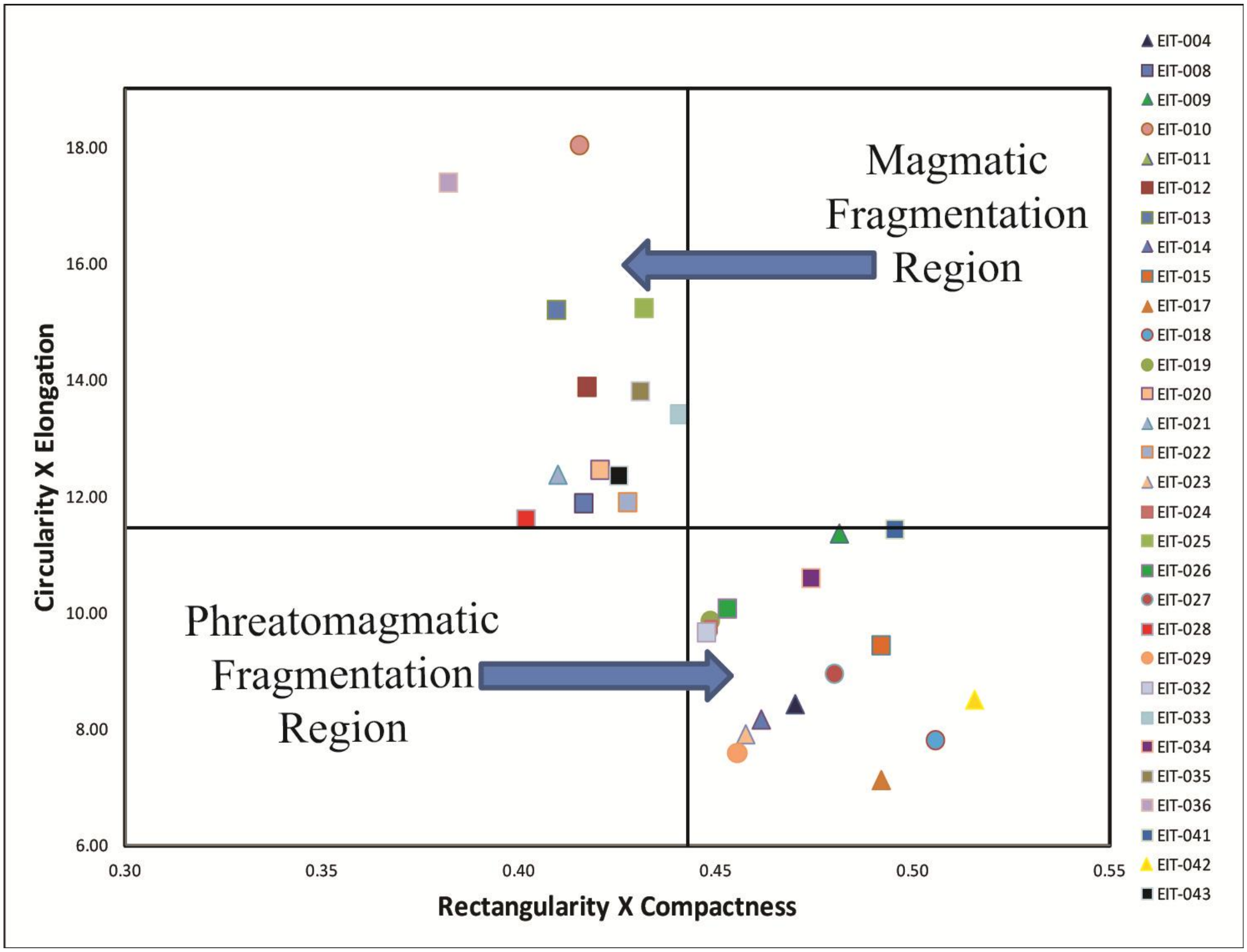

Fig. 15 Average Image Particle Analysis (IPA) values for BSE images of 30 Erebus tephra. Circles represent tephra from phreatomagmatic eruptions, squares are tephra from magmatic eruptions, and triangles are from mixed eruptions.

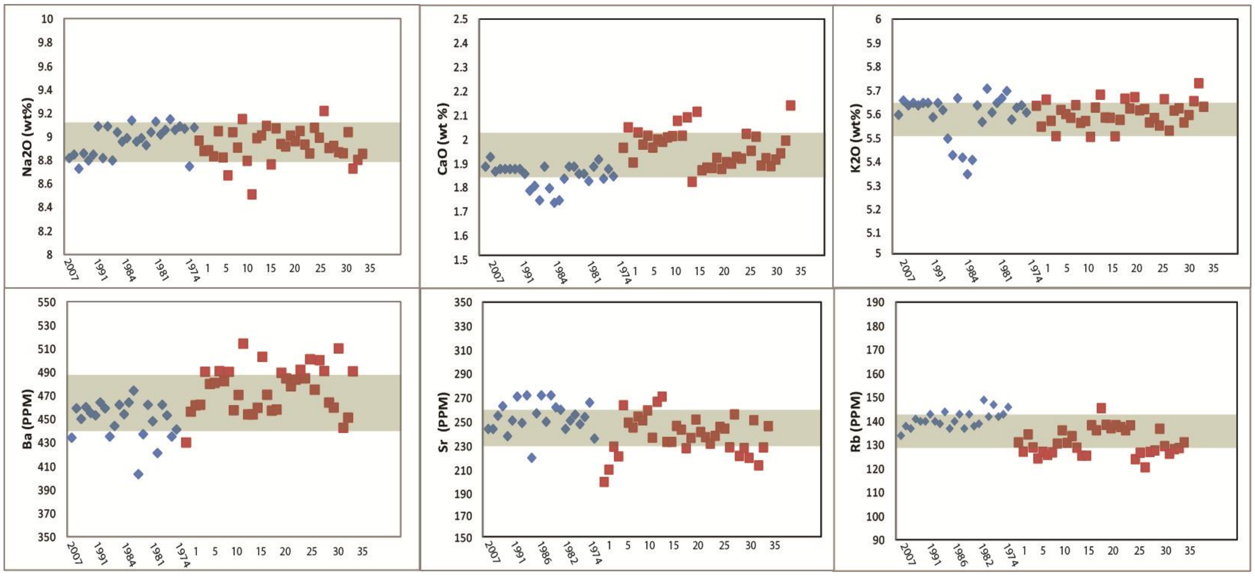

Fig. 16 Time series plot comparing lava lake composition (blue diamonds) to glass from englacial tephra (red squares). The diamonds represent all of the lava samples from 2007 to 1972 from Kelly et al. (2008b). Red Squares are from this study and are presented by sample number. The grey boxes represent one standard deviation in the data for all Erebus glass analyses. For trace elements (Ba, Sr and Rb)-blue diamonds are solution ICP-MS analyses (Kelly et al., 2008b) and red squares are LA-ICP-MS analyses.

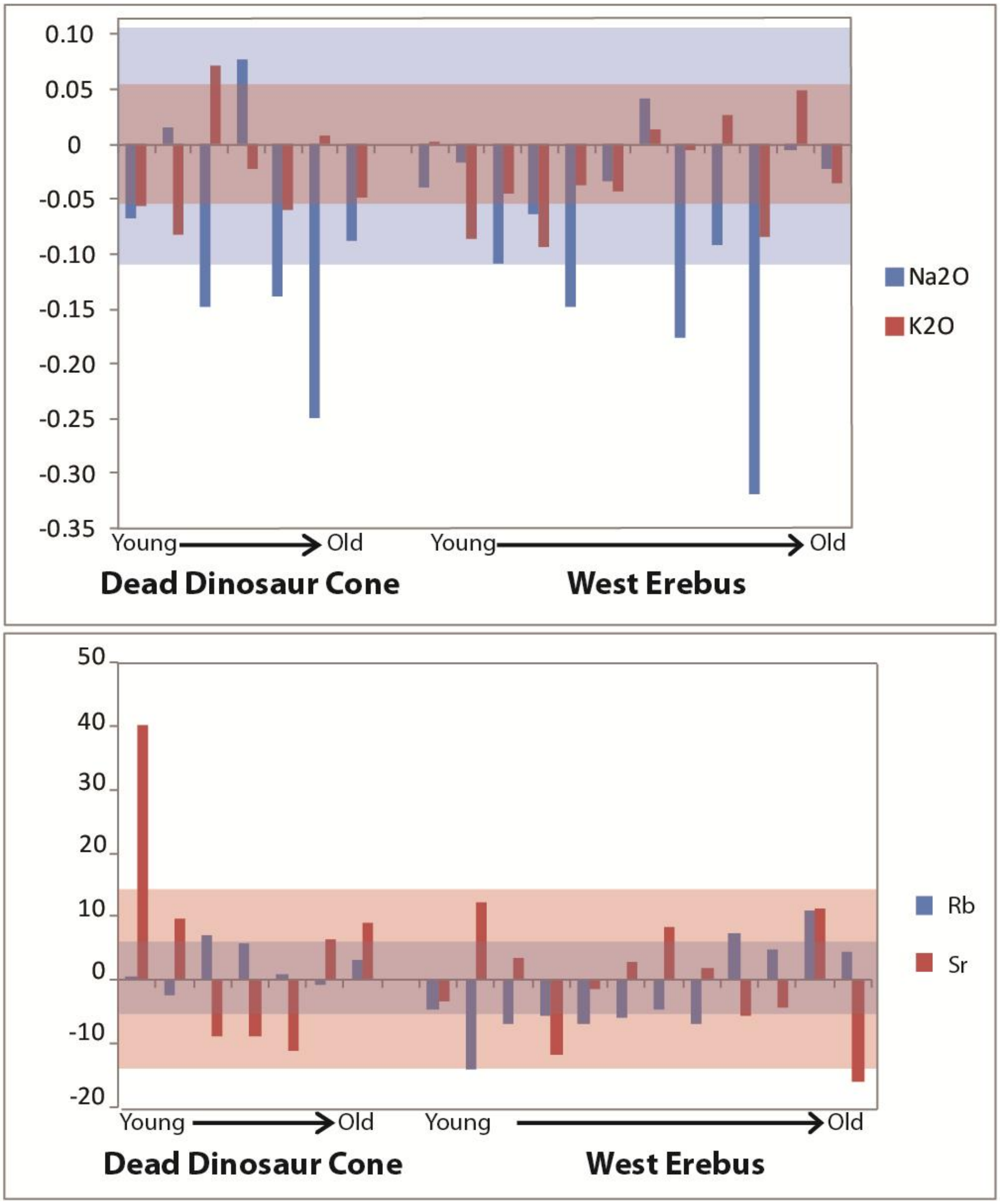

Fig. 17 Plots of K_2O & Na_2O (wt. %) and Sr & Rb (ppm) for Erebus tephra layers on a difference diagram. Zero is the mean composition of Erebus phonolite and bars are deviations from mean in stratigraphic order. The youngest tephra in the stratigraphic section will be on the left and the oldest on the right. The red and blue shaded areas correspond to the 1σ variation in the data for their respective element or oxide

.**Table 1** Textures, vesicularity and inferred eruptive mechanism of Erebus englacial tephra

Vesicularity		Phreatomagmatic Textures										Magmatic Textures						Eruption Type
		Blocky	Platy	Hackly	Mossy	Chipping	Accretionary Lapilli	Hydration Rind	Quench Cracks	Chemical Pitting	Adhering particles	Torn	Pumice	Fluidal Droplets	Welded Droplets	Budding	Pele's Hair	
EIT-001*	Mod	O	A		O						A				O	R	O	Mixed
EIT-003*	Mod		A	O							C	R		O	R		R	Magmatic
EIT-004*	Mod	A	A	C	C	C				R	R		R				O	Mixed
EIT-005*	Mod	O	A	O							A	O			O		O	Mixed
EIT-006*	Poor	C	A	C	O		R		O		A							PM
EIT-007*	Mod		C		O	O			R		O	O					C	Magmatic
EIT-008	Well		C							R	R	A	O	C	O	O	A	Magmatic
EIT-009	Mod	C	C		O		R	O	C	O	A	O					C	Mixed
EIT-010	Mod	C	C		C	O					C	O						PM
EIT-011	Mod	C	C								C	O		R			O	Mixed
EIT-012	Well	O	O									O	O	C	O	O	C	Magmatic
EIT-013	Well		C	O								O	O	R		R		Magmatic
EIT-014	Poor	A	O	O	A					R				R				PM
EIT-015	Mod	A	A	C	O						C		R				R	Mixed
EIT-017	Poor	C	C		A	C					C			O				Mixed
EIT-018	Poor	A	C	C	A	C		C	C		C							PM
EIT-019	Poor	A	A	A	C	C			C		C			R				PM
EIT-020	Well	O	O	O	O		R			O	O			O			C	Mixed
EIT-021	Poor	O	O	O					R		R	R		R			R	Mixed
EIT-022	Well	O		R				C				A	O	O			C	Magmatic
EIT-023	Well	C	O	O							O	C	O	O			C	Mixed
EIT-024	Well		C			O					C	A	R	C		O	A	Magmatic
EIT-025	Well										O	A	O	O			A	Magmatic
EIT-027	Mod	C	C	C		C					R		O				R	Magmatic
EIT-028	Mod		R	R								A					C	Magmatic
EIT-029	Mod	C	R	C		C						O					C	Magmatic
EIT-033	Well	C	C		O				R		C	O					O	Mixed
EIT-034	Well											C	C	C		O	A	Magmatic
EIT-035	Well		C		O			R	R		C	C		C			A	Magmatic
EIT-036	Well					O					O	C	R				O	Magmatic
EIT-041	Well	O	O		R				R	R		C	O				C	Magmatic
EIT-042**	Poor	A	C	C	R	C				R	C			R			R	Mixed
EIT-043	Mod	C	C	O						R		C					O	Mixed

Notes: For Vesicularity: Mod = Moderate vesicularity, Poor= Poor vesicularity, Well=Well vesiculated. Relative abundances: A=abundant, C=common, O=occasional, R= rare. Eruption type: PM= phreatomagmatic eruption. * from Mount Terra Nova; ** EIT-042 from Allan Hills (Manhaul Bay)

	ϕ_{16}	ϕ_{84}	Md (ϕ_{50})	σ_{ϕ}
EIT-013	1.15	2.00	1.54	0.43
EIT-008	2.25	3.40	2.71	0.58
EIT-010	2.60	3.78	3.31	0.59
EIT-015	2.25	3.68	2.83	0.71
EIT-043	2.05	3.48	2.67	0.72
EIT-017	2.05	3.54	2.70	0.75
EIT-012	2.50	4.01	3.61	0.76
EIT-034	1.43	3.01	2.58	0.79
EIT-041	1.64	3.24	2.48	0.80
EIT-018	1.80	3.39	2.56	0.80
EIT-024	1.34	2.96	2.23	0.81
EIT-011	1.92	3.58	2.65	0.83
EIT-025	1.45	3.16	2.40	0.86
EIT-023	1.99	3.78	2.69	0.90
EIT-042*	3.35	5.23	4.03	0.94
EIT-020	1.80	4.34	2.89	1.27
EIT-009	2.13	5.23	3.19	1.55

Table 2 Inman (1952) sorting parameter for the tephra. All data is graphically derived from Fig. 2. Md (ϕ_{50}) represents the phi (ϕ) value for the cumulative wt% of tephra at 50% (ϕ_{50}), which is defined as the median tephra size. ϕ_{16} and ϕ_{84} are the phi values for the cumulative wt% at 16wt% and 84wt%, respectively and help define the sorting (σ_{ϕ}) (Cas and Wright, 1987). * from Allan Hills (Manhaul Bay)

Table 3 Average Image Particle Analysis for all Erebus Tephra

Sample	Rectangularity	σ	Compactness	σ	Circularity	σ	Elongation	σ	RectXComp	σ	CircXElong	σ
EIT-004	0.90	0.09	0.53	0.08	2.55	0.38	3.24	1.01	0.47	0.08	8.44	3.53
EIT-008	0.94	0.12	0.44	0.12	2.94	0.61	3.88	1.31	0.42	0.12	11.89	5.94
EIT-009	0.95	0.15	0.52	0.13	2.81	0.82	3.68	1.89	0.48	0.08	11.37	8.67
EIT-010	1.12	0.24	0.37	0.10	3.81	0.87	4.57	1.37	0.42	0.16	18.04	8.60
EIT-011	0.95	0.14	0.48	0.10	2.85	0.62	3.28	1.41	0.45	0.10	9.78	5.76
EIT-012	0.95	0.08	0.44	0.12	3.01	0.54	4.28	2.35	0.42	0.13	13.89	11.23
EIT-013	0.99	0.12	0.42	0.11	3.21	0.69	4.45	2.29	0.41	0.09	15.22	10.62
EIT-014	0.88	0.06	0.52	0.11	2.52	0.32	3.24	1.08	0.46	0.10	8.18	3.65
EIT-015	0.93	0.09	0.53	0.09	2.67	0.41	3.44	1.08	0.49	0.09	9.45	4.01
EIT-017	2.44	0.49	0.56	0.12	2.93	0.94	0.88	0.11	0.49	0.11	7.14	3.72
EIT-018	2.49	0.35	0.56	0.07	3.04	1.17	0.90	0.09	0.51	0.07	7.82	3.99
EIT-019	2.56	0.32	0.51	0.10	3.75	1.34	0.88	0.09	0.45	0.10	9.87	4.53
EIT-020	2.90	0.60	0.45	0.12	4.02	1.68	0.93	0.08	0.42	0.11	12.47	7.90
EIT-021	2.83	0.56	0.45	0.15	4.14	1.60	0.90	0.08	0.41	0.14	12.38	6.87
EIT-022	2.84	0.66	0.47	0.15	3.85	1.78	0.91	0.08	0.43	0.15	11.91	10.02
EIT-023	2.56	0.35	0.51	0.10	3.01	0.95	0.89	0.06	0.46	0.10	7.93	3.53
EIT-024	2.75	0.48	0.49	0.10	3.40	1.05	0.93	0.08	0.45	0.09	9.77	5.05
EIT-025	3.09	0.79	0.45	0.13	4.47	2.22	0.97	0.15	0.43	0.13	15.25	12.16
EIT-026	2.73	0.41	0.49	0.12	3.55	1.37	0.92	0.09	0.45	0.12	10.09	5.52
EIT-027	2.78	0.37	0.50	0.11	3.16	1.01	0.95	0.10	0.48	0.12	8.97	3.71
EIT-028	2.95	0.51	0.43	0.10	3.86	1.10	0.94	0.13	0.40	0.13	11.62	4.29
EIT-029	2.49	0.38	0.52	0.08	3.00	0.92	0.88	0.09	0.46	0.07	7.59	2.88
EIT-032	2.65	0.43	0.50	0.12	3.52	1.31	0.90	0.12	0.45	0.14	9.67	4.87
EIT-033	3.24	1.05	0.44	0.10	3.86	1.29	1.02	0.23	0.44	0.09	13.42	9.21
EIT-034	1.00	0.16	0.47	0.08	3.02	0.58	3.40	1.04	0.47	0.12	10.61	4.75
EIT-035	3.23	1.05	0.43	0.12	4.08	1.67	1.01	0.29	0.43	0.16	13.82	8.42
EIT-036	3.20	0.57	0.40	0.09	5.04	2.99	0.95	0.07	0.38	0.08	17.40	14.87
EIT-041	0.96	0.27	0.53	0.15	2.83	1.07	3.55	2.20	0.50	0.17	11.45	10.72
EIT-042	0.92	0.12	0.56	0.09	2.54	0.37	3.29	1.12	0.52	0.12	8.52	3.56
EIT-043	0.94	0.11	0.45	0.10	2.92	0.40	4.23	1.52	0.43	0.11	12.37	5.79

Table 4 Mean and standard deviations of major element compositions determined by electron microprobe of glass shards in englacial tephra from flanks of Erebus volcano and Allan Hills (EIT-042)

Sample	EIT-008	σ	EIT-009	σ	EIT-010	σ	EIT-011	σ	EIT-012	σ	EIT-013	σ	EIT-014	σ	EIT-015	σ	EIT-017	σ
N	11		12		11		12		12		12		9		21		8	
SiO2	55.65	0.37	55.94	0.24	55.65	0.36	55.70	0.25	55.47	0.54	55.38	0.37	55.49	0.20	55.52	0.34	55.55	0.33
TiO2	1.01	0.03	1.02	0.05	1.02	0.05	1.04	0.08	1.04	0.06	1.06	0.04	1.03	0.05	1.03	0.05	0.97	0.03
Al2O3	19.73	0.21	19.64	0.17	19.75	0.20	19.68	0.24	19.76	0.22	19.83	0.20	19.69	0.11	19.62	0.17	19.62	0.08
FeO	5.36	0.11	5.31	0.19	5.33	0.13	5.43	0.06	5.32	0.11	5.27	0.12	5.44	0.10	5.38	0.10	5.46	0.12
MnO	0.24	0.02	0.23	0.03	0.26	0.04	0.24	0.03	0.26	0.04	0.24	0.04	0.25	0.03	0.24	0.03	0.25	0.03
MgO	0.87	0.03	0.84	0.04	0.86	0.03	0.89	0.04	0.90	0.02	0.90	0.03	0.93	0.03	0.90	0.05	0.86	0.03
CaO	1.97	0.06	1.91	0.05	1.98	0.16	1.97	0.04	1.99	0.06	2.02	0.04	2.16	0.05	2.02	0.11	1.83	0.08
Na2O	9.00	0.28	8.89	0.29	9.05	0.44	8.83	0.20	9.04	0.38	9.15	0.26	8.68	0.18	8.99	0.32	9.09	0.44
K2O	5.61	0.04	5.66	0.14	5.51	0.13	5.60	0.09	5.64	0.13	5.57	0.12	5.58	0.13	5.63	0.12	5.59	0.13
P2O5	0.28	0.04	0.25	0.04	0.29	0.05	0.29	0.04	0.32	0.02	0.30	0.04	0.30	0.04	0.28	0.05	0.28	0.04
SO2	0.08	0.02	0.07	0.01	0.10	0.02	0.08	0.02	0.08	0.02	0.08	0.02	0.07	0.02	0.08	0.02	0.08	0.02
F	0.23	0.01	0.18	0.09	0.16	0.05	0.19	0.13			0.29	0.00	0.18	0.06	0.21	0.11	0.30	0.12
Cl	0.15	0.01	0.15	0.01	0.16	0.02	0.15	0.01	0.16	0.01	0.14	0.02	0.14	0.01	0.16	0.02	0.15	0.02
Total	100.00		100.00		100.00		100.00		100.00		100.00		100.00		100.00		100.00	

	EIT-019	σ	EIT-020	σ	EIT-021	σ	EIT-022	σ	EIT-023	σ	EIT-024	σ	EIT-025	σ	EIT-026	σ	EIT-027	σ
N	10		10		10		12		12		11		11		11		10	
SiO2	55.66	0.32	55.57	0.18	55.54	0.19	55.52	0.18	55.53	0.17	55.51	0.26	55.56	0.18	55.55	0.18	55.39	0.24
TiO2	1.00	0.04	1.00	0.04	1.01	0.04	1.00	0.03	1.02	0.03	1.01	0.05	1.02	0.04	1.02	0.05	1.03	0.05
Al2O3	19.64	0.10	19.68	0.11	19.61	0.14	19.60	0.13	19.63	0.13	19.56	0.10	19.67	0.12	19.73	0.08	19.69	0.09
FeO	5.43	0.10	5.45	0.11	5.49	0.10	5.40	0.13	5.34	0.21	5.37	0.09	5.40	0.09	5.40	0.14	5.39	0.07
MnO	0.27	0.05	0.29	0.05	0.28	0.04	0.26	0.01	0.29	0.02	0.28	0.03	0.26	0.05	0.27	0.02	0.27	0.04
MgO	0.85	0.03	0.86	0.04	0.87	0.02	0.89	0.03	0.86	0.03	0.87	0.02	0.87	0.04	0.89	0.03	0.91	0.04
CaO	1.88	0.06	1.89	0.03	1.88	0.06	1.93	0.04	1.88	0.12	1.91	0.07	1.90	0.05	1.93	0.06	1.92	0.06
Na2O	9.07	0.35	8.94	0.25	8.92	0.23	9.01	0.27	8.96	0.21	9.05	0.22	8.94	0.16	8.86	0.24	9.08	0.11
K2O	5.51	0.25	5.58	0.13	5.67	0.05	5.63	0.06	5.67	0.12	5.62	0.10	5.62	0.07	5.57	0.10	5.59	0.10
P2O5	0.28	0.04	0.27	0.04	0.28	0.05	0.27	0.05	0.28	0.06	0.28	0.06	0.27	0.02	0.28	0.05	0.27	0.04
SO2	0.08	0.02	0.08	0.01	0.08	0.02	0.08	0.02	0.07	0.02	0.07	0.02	0.08	0.02	0.08	0.02	0.07	0.02
F	0.21	0.05	0.22	0.08	0.23	0.11	0.27	0.08	0.30	0.10	0.30	0.10	0.26	0.08	0.27	0.08	0.26	0.10
Cl	0.16	0.02	0.16	0.04	0.14	0.01	0.15	0.02	0.15	0.01	0.15	0.01	0.14	0.02	0.15	0.02	0.14	0.01
Total	100.00		100		100		100		100		100		100		100		100	

	EIT-028	σ	EIT-029	σ	EIT-032	σ	EIT-033	σ	EIT-034	σ	EIT-035	σ	EIT-036	σ
N	11		9		11		10		12		11		11	
SiO2	55.34	0.28	55.13	0.21	55.50	0.47	55.39	0.26	55.89	0.36	55.65	0.25	55.45	0.22
TiO2	1.05	0.05	1.04	0.04	1.02	0.08	1.02	0.05	1.00	0.06	1.01	0.03	1.01	0.04
Al2O3	19.73	0.15	19.52	0.19	19.53	0.30	19.68	0.14	19.67	0.23	19.64	0.12	19.68	0.14
FeO	5.33	0.08	5.47	0.10	5.61	0.22	5.45	0.10	5.35	0.09	5.44	0.08	5.45	0.13
MnO	0.27	0.05	0.28	0.05	0.28	0.05	0.28	0.05	0.27	0.03	0.29	0.04	0.30	0.03
MgO	0.91	0.02	0.86	0.04	0.88	0.06	0.88	0.02	0.85	0.05	0.87	0.02	0.85	0.03
CaO	2.03	0.15	1.96	0.08	2.01	0.08	1.89	0.05	1.93	0.05	1.89	0.06	1.92	0.07
Na2O	8.99	0.19	9.22	0.17	8.91	0.22	8.92	0.20	8.87	0.28	8.86	0.12	9.04	0.17
K2O	5.56	0.11	5.67	0.16	5.53	0.10	5.62	0.13	5.63	0.07	5.57	0.12	5.60	0.11
P2O5	0.28	0.04	0.32	0.05	0.29	0.05	0.31	0.04	0.27	0.06	0.29	0.04	0.28	0.05
SO2	0.08	0.02	0.06	0.03	0.07	0.02	0.08	0.02	0.08	0.02	0.07	0.02	0.06	0.02
F	0.28	0.20	0.32	0.08	0.23	0.11	0.31	0.07	0.06	0.11	0.26	0.08	0.23	0.09
Cl	0.14	0.02	0.14	0.01	0.14	0.01	0.15	0.01	0.15	0.02	0.15	0.02	0.14	0.01
Total	100		100		100		100		100		100		100	

	EIT-041	σ	EIT-042*	σ	EIT-043	σ	Mean	σ	%RSD	Kelly et al. 2008	σ
N	11		9		11		433				
SiO2	55.63	0.14	55.62	0.25	55.34	0.17	55.60	0.28	0.51	55.74	0.18
TiO2	1.07	0.03	0.99	0.06	1.08	0.04	1.03	0.04	4.21	1.02	0.03
Al2O3	19.74	0.12	19.49	0.14	19.61	0.11	19.57	0.20	1.00	19.64	0.13
FeO	5.42	0.12	5.58	0.12	5.41	0.09	5.44	0.09	1.60	5.31	0.2
MnO	0.28	0.04	0.27	0.03	0.28	0.04	0.28	0.03	9.15	0.27	0.02
MgO	0.85	0.03	0.84	0.03	0.90	0.03	0.86	0.07	8.31	0.80	0.03
CaO	1.95	0.05	2.00	0.08	2.14	0.05	2.01	0.21	10.37	1.86	0.05
Na2O	8.73	0.15	8.80	0.24	8.86	0.12	8.90	0.18	1.98	9.09	0.1
K2O	5.66	0.08	5.73	0.16	5.63	0.09	5.58	0.10	1.74	5.57	0.08
P2O5	0.26	0.04	0.28	0.04	0.29	0.06	0.29	0.02	8.28	0.28	0.03
SO2	0.08	0.02	0.08	0.02	0.08	0.02	0.08	0.01	9.73	0.08	0.02
F	0.18	0.07	0.15	0.08	0.22	0.09	0.21	0.09	40.59	0.28	0.08
Cl	0.16	0.01	0.16	0.01	0.15	0.01	0.15	0.01	8.12	0.15	0.01
Total	100		100		100					100	

Notes: All EMP analysis were performed on a Cameca SX-100 electron microprobe (EMP) at New Mexico Tech. * Distal Tephra from Allan Hills. Glass shards were analyzed using a defocused 20μm beam at 15keV and 10nA to reduce Na volatilization. Count times = 20s except S= 30s, Cl=40 and F=60. FeO is total Fe. N= number of analyses averaged Between 8 and 21 shards were analyzed for each tephra and the data was normalized to 100% and mean values are reported here. Samples geochemically similar to Erebus phonolite are averaged together to give the average composition of Erebus glass (EIT-004, EIT-006, EIT-008 to EIT-043). Error for all Erebus glass is at 1σ. %RSD= relative standard deviation at 1σ. Analytical precision from microprobe analyses is calculated by standard deviation of replicate analyses of standards VG568, G2, KE-12, kaersuitite (357), hornblende (Kak) and orthoclase (374). Mean and standard deviation values for VG568: SiO_2= 76.59, 0.26; TiO_2= 0.08, 0.03; Al_2O_3=12.01, 0.15; FeO= 1.16, 0.12; CaO= 0.44, 0.04; MgO= 0.02, 0.01; MnO= 0.03, 0.02; Na_2O=3.80, 0.12; K_2O=4.91, 0.10; SO_2=0.01, 0.02; P_2O_5=0.02, 0.02; Cl= 0.11, 0.02; F=0.14, 0.09; Total= 99.31, 0.29. Mean and standard deviation values for KE12: SiO_2= 70.37, 0.30; TiO_2= 0.30, 0.03; Al_2O_3=7.56, 0.15; FeO= 8.51, 0.10; CaO= 0.38, 0.02; MgO= 0.01, 0.01; MnO= 0.30, 0.03; Na_2O=6.80, 0.69; K_2O=4.38, 0.09; SO_2=0.04, 0.02; P_2O_5=0.02, 0.02; Cl= 0.31, 0.04; F=0.39, 0.09; Total= 99.36, 0.91. Certified values for KE12 and VG568 can be found at http://geoinfo.nmt.edu/labs/microprobe/home.html.

Table 5 Trace element compositions of glass shards in englacial tephra from the flanks of Erebus volcano

	EIT-008		EIT-009		EIT-010		EIT-011		EIT-012		EIT-013		EIT-014		EIT-015	
	Mean	σ	Mean	σ	Mean	σ	Mean	σ	Mean	σ	Mean	σ	Mean	σ	Mean	σ
Rb	131	4	134	3	125	5	126	2	131	4	132	3	129	3	129	5
Sr	201	16	231	17	250	26	250	11	252	18	235	12	272	22	232	13
Y	69.4	4.3	69.9	2.7	77.8	3.2	77.7	4.0	78.3	3.0	64.5	2.9	66.8	1.2	68.4	4.6
Zr	1589	97	1601	69	1684	33	1657	44	1678	49	1495	67	1416	18	1522	91
Nb	444	16	441	22	435	8	435	10	443	15	440	23	395	10	424	15
Cs	1.70	0.19	1.73	0.18	1.60	0.23	1.56	0.13	1.67	0.15	1.82	0.14	1.75	0.09	1.76	0.15
Ba	442	25	467	26	491	41	479	17	483	18	458	32	515	35	459	20
La	162	9	162	6	166	4	163	5	168	8	153	8	148	4	154	8
Ce	288	11	285	16	277	10	279	7	279	12	272	11	282	5	268	13
Pr	31.6	1.9	30.9	1.6	30.8	1.3	30.8	1.1	31.0	1.6	29.4	1.6	30.0	0.7	30.0	1.7
Nd	105	8	105	7	110	5	109	6	114	3	101	6	101	4	102	5
Sm	17.5	0.8	16.9	1.3	19.0	1.4	18.2	1.7	17.8	1.9	16.5	1.1	16.5	1.4	17.6	1.5
Eu	2.91	0.33	3.49	0.28	3.49	0.40	3.44	0.37	3.33	0.37	3.01	0.31	3.15	0.17	2.99	0.37
Tb	2.40	0.26	2.17	0.20	2.45	0.19	2.29	0.22	2.52	0.27	2.27	0.20	1.92	0.22	2.25	0.27
Dy	13.1	1.1	14.0	1.2	14.1	0.9	14.4	0.9	14.7	1.2	12.7	0.7	11.8	0.8	13.4	1.0
Ho	2.60	0.33	2.64	0.22	2.52	0.19	2.69	0.13	2.88	0.24	2.52	0.21	2.53	0.35	2.47	0.22
Er	6.70	0.48	7.25	0.77	8.05	1.18	7.82	0.84	8.74	0.66	6.36	0.85	6.42	0.48	6.94	0.73
Tm	1.13	0.20	1.18	0.24	1.15	0.13	1.21	0.15	1.15	0.13	1.06	0.09	1.07	0.11	1.11	0.17
Yb	7.92	0.70	8.11	0.95	8.35	1.28	8.52	0.79	8.84	0.73	7.80	0.84	7.79	0.80	7.50	0.75
Lu	1.11	0.16	1.17	0.16	1.22	0.14	1.22	0.11	1.28	0.12	1.09	0.13	1.02	0.12	1.13	0.17
Hf	29.6	2.1	31.5	1.7	31.2	2.2	31.2	1.9	32.7	3.1	27.9	2.4	26.5	2.0	28.8	2.1
Ta	25.9	1.4	25.9	2.0	26.6	1.7	26.8	1.1	27.6	1.7	24.9	1.7	23.1	1.2	23.9	2.3
Pb	7.14	0.42	7.16	0.44	6.59	0.57	6.28	0.40	6.95	0.77	7.22	0.95	6.75	0.53	7.03	0.85
Th	31.0	2.2	30.9	2.6	32.6	1.3	32.4	1.2	32.7	1.5	29.6	1.8	27.8	0.5	28.9	2.2
U	8.29	0.52	7.89	0.37	7.44	0.48	7.52	0.37	7.38	0.34	7.86	0.42	7.73	0.34	7.47	0.68

	EIT-017			EIT-018		EIT-019		EIT-020		EIT-021		EIT-022		EIT-023		EIT-024	
	Mean	σ		Mean	σ	Mean	σ	Mean	σ	Mean	σ	Mean	σ	Mean	σ	Mean	σ
Rb	139	3	Rb	114	41	136	3	146	5	139	6	137	4	139	3	138	4
Sr	256	31	Sr	618	901	244	12	229	20	238	23	253	11	243	12	238	11
Y	75.2	5.6	Y	61.7	25.1	77.7	2.1	73.8	8.0	73.5	3.8	72.0	2.3	79.7	3.0	79.1	3.7
Zr	1551	81	Zr	1270	498	1586	33	1567	123	1534	51	1517	44	1703	54	1685	76
Nb	400	23	Nb	316	116	402	8	405	33	400	15	407	8	410	8	415	11
Cs	1.97	0.37	Cs	1.44	0.54	1.75	0.10	1.81	0.17	1.79	0.18	1.74	0.13	1.79	0.12	1.78	0.28
Ba	460	31	Ba	577	210	471	19	458	43	459	18	490	22	485	18	479	16
La	161	12	La	133	44	165	8	163	16	159	5	158	4	170	5	168	6
Ce	291	16	Ce	236	82	296	11	302	11	290	7	294	8	296	6	303	8
Pr	31.1	1.7	Pr	26.1	9.2	32.2	1.6	31.8	2.6	31.1	1.1	30.8	1.0	32.4	1.2	32.7	0.9
Nd	105	6	Nd	92	32	110	8	108	11	106	6	105	4	113	8	115	1
Sm	17.4	1.8	Sm	15.7	5.8	18.3	1.5	17.5	2.8	17.5	1.5	16.8	1.5	18.0	1.9	17.9	1.4
Eu	3.63	0.30	Eu	3.37	0.42	3.44	0.40	3.27	0.51	3.23	0.29	3.33	0.39	3.57	0.31	3.32	0.18
Tb	2.26	0.28	Tb	1.91	0.74	2.31	0.18	2.23	0.43	2.23	0.20	2.26	0.23	2.50	0.19	2.39	0.22
Dy	13.7	1.1	Dy	11.4	4.3	14.6	1.4	14.0	1.0	13.0	1.4	12.9	1.0	14.4	1.3	14.4	1.0
Ho	2.76	0.40	Ho	2.17	0.83	2.85	0.40	2.79	0.12	2.71	0.30	2.60	0.26	2.93	0.29	2.80	0.31
Er	7.18	0.81	Er	6.36	2.52	7.61	0.97	7.78	0.92	7.77	0.44	7.43	0.55	7.88	0.74	7.89	0.52
Tm	1.15	0.11	Tm	0.96	0.37	1.16	0.15	1.07	0.18	1.09	0.17	1.12	0.16	1.25	0.15	1.27	0.21
Yb	8.26	0.97	Yb	6.96	2.87	8.68	0.91	8.34	0.77	7.76	0.82	8.07	0.42	9.35	0.85	8.47	0.80
Lu	1.07	0.12	Lu	1.05	0.42	1.27	0.09	1.24	0.15	1.25	0.12	1.12	0.08	1.30	0.22	1.31	0.17
Hf	30.7	2.6	Hf	24.3	10.1	31.5	2.4	31.2	2.6	28.6	2.0	28.5	1.9	32.5	1.9	31.6	1.7
Ta	23.7	2.4	Ta	19.5	7.3	24.7	0.8	25.4	3.4	24.0	0.9	24.0	1.0	25.5	0.9	25.7	0.4
Pb	7.28	0.93	Pb	8.37	6.15	6.25	0.40	10.47	3.65	7.16	0.43	6.83	0.42	8.04	2.08	7.03	0.38
Th	30.5	2.5	Th	25.7	9.5	31.9	1.7	30.5	3.8	30.4	1.3	29.6	1.4	32.2	1.2	32.6	0.6
U	7.91	0.99	U	6.58	2.47	8.37	0.43	8.68	0.78	8.16	0.32	8.93	2.52	8.33	0.35	8.64	0.41

	EIT-025		EIT-026		EIT-027		EIT-028		EIT-029		EIT-032		EIT-033		EIT-034	
	Mean	σ	Mean	σ	Mean	σ	Mean	σ	Mean	σ	Mean	σ	Mean	σ	Mean	σ
Rb	136	7	139	5	124	3	127	7	121	11	127	4	128	5	136	5
Sr	233	21	239	7	247	14	245	17	230	31	257	13	223	12	229	9
Y	66.5	3.9	71.6	2.0	79.3	3.8	72.8	4.6	75.6	6.1	65.9	2.6	66.5	2.9	69.5	2.0
Zr	1483	9	1524	35	1681	35	1605	43	1652	58	1478	47	1522	65	1531	44
Nb	415	12	417	6	423	7	427	10	420	9	413	11	425	9	446	10
Cs	1.86	0.23	1.77	0.11	1.56	0.15	1.73	0.13	1.55	0.13	1.85	0.21	1.67	0.20	1.78	0.29
Ba	484	17	493	23	486	27	502	21	476	46	501	12	492	17	461	20
La	150	2	156	4	166	2	159	5	167	7	153	3	156	2	155	6
Ce	279	6	290	6	273	5	278	8	282	8	273	9	288	4	277	7
Pr	29.3	0.4	29.8	1.1	31.1	0.8	31.3	1.7	32.1	0.9	29.5	1.3	29.6	0.6	30.4	1.0
Nd	98	4	103	6	112	4	106	7	112	3	103	3	101	7	104	4
Sm	16.1	1.4	18.0	1.0	17.8	1.6	18.0	1.9	18.3	1.5	17.5	1.6	16.9	1.0	16.8	0.9
Eu	3.03	0.30	3.48	0.60	3.23	0.31	3.56	0.47	3.30	0.16	3.07	0.30	3.18	0.31	3.35	0.29
Tb	2.34	0.31	2.19	0.14	2.53	0.23	2.44	0.18	2.93	0.43	2.28	0.12	2.05	0.23	2.34	0.23
Dy	12.0	1.3	13.2	1.6	15.3	1.7	13.0	1.8	13.9	2.1	12.7	1.0	13.2	1.6	13.1	0.5
Ho	2.48	0.33	2.63	0.27	2.78	0.21	2.52	0.27	2.65	0.29	2.23	0.35	2.39	0.21	2.50	0.16
Er	6.63	0.59	8.16	1.54	9.05	0.39	7.91	0.74	8.27	0.88	7.08	0.61	7.28	0.80	7.71	0.43
Tm	1.14	0.17	0.98	0.09	1.23	0.17	1.27	0.14	1.24	0.21	0.92	0.22	1.07	0.20	1.12	0.14
Yb	6.99	0.56	7.49	0.46	8.69	0.71	8.82	1.17	8.51	0.70	7.44	0.58	8.00	0.74	7.84	0.50
Lu	1.03	0.12	1.21	0.11	1.31	0.19	1.10	0.12	1.30	0.12	1.10	0.16	1.03	0.20	1.11	0.19
Hf	26.8	1.5	29.6	1.4	33.0	2.3	30.5	1.9	32.5	2.1	29.0	0.9	29.4	1.5	29.0	2.1
Ta	24.0	1.1	24.9	1.0	26.5	1.1	25.8	0.9	25.9	0.9	23.6	1.2	24.5	1.3	25.3	1.0
Pb	6.79	0.75	7.05	0.70	6.33	0.59	6.64	0.96	6.04	0.57	7.45	0.94	6.64	0.97	7.21	0.61
Th	28.1	1.1	29.3	1.0	33.2	1.0	32.1	0.8	32.3	1.4	29.2	1.3	29.9	1.8	29.7	1.1
U	7.92	0.56	8.09	0.33	7.31	0.21	7.37	0.45	7.71	0.30	7.52	0.25	7.90	0.40	7.85	0.28

	EIT-035		EIT-036		EIT-041		EIT-042*		EIT-043		Erebus		81003G**	81003	
	Mean	σ	Mean	σ	Mean	σ	Mean	σ	Mean	σ	Total	σ	Mean	Mean	σ
Rb	130	8	127	5	129	4	129	3	131	3	127	7	138	136	4
Sr	221	11	252	31	215	18	213	63	247	22	243	72	261	247	10
Y	75.4	5.9	76.5	4.0	71.7	3.9	78.6	4.4	62.9	2.5	69.9	5.4	76.3	68.9	4.7
Zr	1660	26	1646	62	1516	42	1591	62	1395	25	1511	100	1592	1469	98
Nb	423	12	422	8	411	12	419	9	408	10	403	24	414	422	26
Cs	2.01	0.26	1.57	0.25	1.60	0.16	1.56	0.16	1.88	0.18	1.67	0.13	1.79	1.70	0.13
Ba	461	16	511	41	443	26	452	29	491	21	464	27	460	490	24
La	167	5	166	5	155	6	169	7	142	4	154	9	153	151	7
Ce	289	11	294	13	276	8	302	6	275	7	274	13	294	282	10
Pr	32.9	1.0	31.7	1.7	30.5	1.2	33.4	1.6	29.0	1.0	29.8	1.5	31.6	30.2	1.5
Nd	108	7	111	9	105	4	115	7	98	5	103	6	103	101	7
Sm	19.2	1.4	19.3	2.6	17.7	1.0	18.1	1.4	16.3	1.3	17.0	0.9	17.7	17.0	1.3
Eu	3.34	0.51	3.58	0.45	2.92	0.36	3.39	0.37	3.08	0.40	3.18	0.21	3.56	3.34	0.30
Tb	2.19	0.36	2.19	0.40	2.24	0.19	2.33	0.21	2.05	0.08	2.22	0.20	2.24	2.17	0.29
Dy	15.1	1.4	15.2	1.3	14.0	1.1	14.3	1.2	12.3	0.8	13.13	1.02	12.70	12.96	1.43
Ho	2.79	0.30	2.69	0.21	2.80	0.12	2.83	0.29	2.35	0.20	2.54	0.19	2.56	2.53	0.25
Er	7.40	1.11	8.10	1.10	7.52	0.62	8.23	0.59	6.36	0.63	7.26	0.71	7.39	7.23	0.80
Tm	1.26	0.32	1.08	0.04	1.17	0.11	1.23	0.11	1.01	0.10	1.10	0.09		1.05	0.13
Yb	8.55	0.68	9.08	1.19	8.10	1.12	8.32	0.46	7.29	0.57	7.86	0.59	7.16	7.76	0.84
Lu	1.30	0.13	1.36	0.20	1.14	0.09	1.20	0.11	1.14	0.13	1.14	0.10	1.12	1.16	0.21
Hf	32.0	2.4	32.0	1.5	29.9	1.5	31.1	1.5	25.7	1.4	29.0	2.2	31.3	28.2	2.4
Ta	26.5	1.3	26.3	1.4	25.3	1.2	25.4	1.2	23.8	0.7	24.2	1.5	23.1	24.6	1.8
Pb	7.95	0.42	7.44	1.65	6.92	0.65	6.89	0.68	7.11	0.39	6.90	0.82	6.06	7.41	0.64
Th	32.4	0.9	32.9	1.7	30.7	1.5	31.6	1.3	28.5	1.3	29.6	1.8	29.8	28.6	1.9
U	7.51	0.90	7.90	0.41	7.97	0.39	7.73	0.36	7.95	0.43	7.60	0.48	8.78	8.10	0.39

Notes: Trace elements were analyzed by LA-ICP-MS at Aberystwyth University, UK. When possible, analyses were performed on the same tephra shards at the EMP analyses. All data is in ppm and error are given at 1 σ. * Tephra from Allan Hills. ** Glass composition of recently erupted bombs (Kelly et al., 2008b) by solution ICP-MS. 81003 is the same glass as 81003G analyze by Kelly et al., (2008b) but this time analyzed by LA-ICP-MS. Precision of measurements were determined by two different analyses of 81003 (N=40).

Table 6 Average major and trace element compositions of glass shards in englacial tephra from the summit of Mount Terra Nova

	EIT-001b		EIT-003		EIT-004		EIT-005a		EIT-005b		EIT-005c		EIT-006		EIT-007	
N	4	σ	10	σ	8	σ	3	σ	3	σ	2	σ	11	σ	6	σ
SiO2	55.74	0.38	45.54	0.36	55.42	0.40	56.04	0.29	62.6	0.36	63.12	0.03	56.09	0.16	63.12	0.51
TiO2	1.04	0.06	3.62	0.16	1.01	0.04	0.98	0.05	0.38	0.02	0.56	0.00	0.98	0.05	0.50	0.05
Al2O3	19.82	0.26	15.87	0.14	19.59	0.13	19.58	0.04	13.85	0.29	14.82	0.18	19.66	0.27	13.82	0.13
FeO	5.50	0.23	11.09	0.20	5.40	0.10	5.43	0.11	9.24	0.15	8.44	0.08	5.35	0.13	8.89	0.27
MnO	0.23	0.04	0.21	0.04	0.25	0.04	0.24	0.04	0.27	0.03	0.28	0.01	0.25	0.03	0.29	0.04
MgO	0.89	0.05	5.61	0.16	0.92	0.04	0.87	0.01	0.00	0.00	0.06	0.01	0.87	0.04	0.02	0.01
CaO	2.13	0.19	11.7	0.26	2.03	0.10	1.85	0.04	0.89	0.02	1.86	0.03	1.92	0.08	1.15	0.09
Na2O	8.33	0.49	4.08	0.15	8.97	0.23	8.96	0.36	7.51	0.33	5.80	0.13	8.71	0.25	6.90	0.57
K2O	5.62	0.39	1.44	0.04	5.58	0.16	5.55	0.03	4.46	0.07	4.67	0.12	5.46	0.27	4.68	0.15
P2O5	0.33	0.02	0.67	0.07	0.27	0.04	0.23	0.05	0.06	0.05	0.08	0.01	0.28	0.04	0.05	0.03
SO2	0.08	0.04	0.10	0.03	0.09	0.02	0.09	0.02	0.11	0.02	0.09	0.02	0.09	0.02	0.09	0.03
F	0.24	0.01			0.24	0.09							0.31	0.07	0.25	0.09
Cl	0.14	0.01	0.07	0.01	0.16	0.02	0.19	0.05	0.40	0.14	0.22	0.03	0.19	0.05	0.3	0.06
Total	100		100		100		100		100		100		100		100	
Rb			26.3	2.42	133	3							131	3		
Sr			923	87	232	19							219	20		
Y			33.6	3.3	52.1	1.0							62	2		
Zr			292	30	1060	14							1280	39		
Nb			66.3	5.9	346	9							355	10		
Cs			0.49	0.20	1.82	0.10							1.57	0.20		
Ba			371	44	445	30							421	20		
La			52.2	6.4	122	3							141	3		
Ce			87.7	6.3	246	4							262	6		
Pr			12.0	1.2	24.9	0.6							27.5	1.2		
Nd			48.7	3.2	84.8	3.3							95.6	3.2		
Sm			10.1	1.0	14.6	0.6							15.7	1.2		
Eu			3.16	0.39	2.80	0.15							3.12	0.36		
Tb			1.14	0.25	1.53	0.18							1.88	0.15		
Dy			6.65	1.08	9.89	0.70							12.2	0.9		
Ho			1.30	0.15	1.94	0.24							2.60	0.22		
Er			3.61	0.27	5.53	0.42							6.80	0.56		
Tm			0.35	0.09	0.96	0.10							1.11	0.12		
Yb			3.39	0.43	6.47	0.66							7.31	0.57		
Lu			0.49	0.18	0.87	0.11							1.10	0.15		
Hf			5.78	1.20	21.8	1.2							27.6	1.7		
Ta			4.06	0.43	20.8	1.1							23.6	0.6		
Pb			11.1	3.97	6.03	0.47							5.86	0.5		
Th			5.41	0.61	23.0	0.4							27.8	1.2		
U			1.17	0.21	7.22	0.31							7.47	0.23		

Notes: All EMP analysis were performed on a Cameca SX-100 electron microprobe (EMP) at New Mexico Tech. Glass shards were analyzed using a defocused 10, 15 and 20µm beam at 15keV and 10nA to reduce Na volatilization. Count times = 20s except S= 30s, Cl=40 and F=60. FeO is total Fe. N= number of analyses averaged. Between 2 and 11 shards were analyzed for each tephra and the data was normalized to 100%. Mean and standard deviations are reported here. Some tephra are heterogeneous and the individual glass populations are averaged separately denoted with a ‘a,b or c’ after the sample number. Samples that are geochemically similar to Erebus phonolite (EIT-004 and EIT-006) are averaged with Table 1 to give an average value for Erebus phonolite. Analytical precision from microprobe analyses is calculated by standard deviation of replicate analyses of standards VG568, G2g, KE-12, kaersutite (357), hornblende (Kak) and orthoclase (374). Trace elements were analyzed by LA-ICP-MS at Aberystwyth University, UK. When possible, analyses were performed on the same tephra shards as the EMP analyses. All trace element data are in ppm and errors are shown at 1σ. Values were reduced in the same manner as major elements.

Table 7 Comparison of Antarctic trachytes

	N	SiO2	TiO2	Al2O3	FeO	MnO	MgO	CaO	Na2O	K2O	P2O5	SO2	F	Cl
EIT-005b		62.60	0.38	13.85	9.24	0.27	0.00	0.89	7.51	4.46	0.06	0.11		0.4
EIT-005c		63.12	0.56	14.82	8.44	0.28	0.06	1.86	5.80	4.67	0.08	0.09		0.22
EIT-007		63.12	0.50	13.82	8.89	0.29	0.02	1.15	6.90	4.68	0.05	0.09	0.25	0.30
BIT-152		62.57	0.52	13.88	8.84	0.26	0.00	1.03	7.69	4.69	0.04	0.08	0.18	0.20
Mt. Berlin min	36	60.50	0.19	12.47	5.94	0.16	0.00	0.72	6.42	4.16	0.02	0.03	0.10	0.10
Mt. Berlin max		65.11	0.57	16.87	9.04	0.32	0.15	1.78	9.24	5.21	0.13	0.10	0.37	0.27
Mt.Takahe min	7	61.11	0.50	14.05	7.16	0.26	0.05	1.09	5.90	4.60	0.09	0.08	0.07	0.10
Mt. Takahe max		62.28	0.82	15.41	8.97	0.37	0.52	1.62	8.24	5.17	0.16	0.13	0.25	0.10
Mt. Melbourne min	16	57.98	0.13	13.20	3.87	0.11	0.02	0.60	4.58	4.05				
Mt. Melbourne max		68.70	0.88	18.03	12.66	0.68	0.91	2.43	9.80	5.27				

Notes: Comparison of trachytes from Mt. Terra Nova Summit (this study) to trachyitic source volcanoes. The compositional ranges are given for Mt. Berlin (Dunbar et al., 2008), Mt. Takahe (Dunbar, unpublished data) and Mt. Melbourne (Narcisi et al., 2012). N refers to the number of tephra layers used to create the composition range of trachytes.

Table 8 Comparison of distal Erebus tephra

Sample	SiO2	TiO2	Al2O3	FeO	MnO	MgO	CaO	Na2O	K2O	P2O5	SO2	F	Cl	Total
EIT-042	55.62	0.99	19.49	5.58	0.27	0.84	2.00	8.80	5.73	0.28	0.08	0.17	0.16	100
σ	0.22	0.05	0.15	0.11	0.03	0.03	0.09	0.24	0.17	0.04	0.02	0.06	0.01	
BIT-42 (MB)	54.53	0.99	19.74	5.53	0.24	0.83	1.96	8.97	5.57	0.26	0.08	0.23	0.16	100
σ	0.23	0.04	0.14	0.11	0.05	0.04	0.10		0.21	0.04	0.03	0.08	0.01	
BIT-272 (DW)	55.26	0.95	19.41	5.88	0.28	0.80	1.90	8.70	5.48	0.24	0.08	0.18	0.13	100
σ	0.27	0.04	0.07	0.09	0.05	0.01	0.04		0.15	0.04	0.02	0.08	0.01	
BIT-288 (DW)	55.33	0.95	19.43	5.84	0.26	0.80	1.92	8.65	5.49	0.26	0.09	0.20	0.14	100
σ	0.23	0.04	0.09	0.12	0.04	0.03	0.04		0.06	0.04	0.03	0.09	0.02	
TD504	58.40	1.00	18.60	4.50	0.50	1.00	1.60	9.60	4.90					96.40
σ	1.90	0.70	1.10	0.90	0.40	0.70	0.80	0.90	0.60					

Notes: EIT-042 is the distal tephra layer analyzed in this study. The BIT samples are tephra layers from the Transantarctic Mountains analyzed by Harpel et al. (2008). BIT-42 and EIT-042 are the same tephra layer. MB= Manhaul Bay, DW= Mt. DeWitt. TD504 is the speculated Erebus tephra found in Talos Dome ice core by Narcisi et al. (2012).